Intermediate-depth Circulation of the Indian and South Pacific Oceans Measured by Autonomous Floats

Russ E. Davis

Scripps Institution of Oceanography, La Jolla, California, 92093

ABSTRACT: As part of the World Ocean Circulation Experiment, 306 autonomous floats were deployed in the tropical and South Pacific Ocean and 228 were deployed in the Indian Ocean to observe the basin-wide circulation near 900 m depth. Mean velocities, seasonal variability, and lateral eddy diffusivity from the resultant 2583 float-years of data are presented. Area averages, local function fits and a novel application of objective mapping are used to estimate the mean circulation. Patterns of mean circulation resemble those at the surface in both basins. Well-developed subtropical gyres, twice as strong in the Indian Ocean as the Pacific, feed western boundary currents. Tropical gyres are separated by eastward flow along the equator in both hemispheres of both basins, although the Indian subcontinent splits the North Indian tropical gyre. The Antarctic Circumpolar Current (ACC) and West Wind Drifts are prominent in both basins, generally tending slightly southward but deviating to the north behind the Del Cano, Kerguelen and Campbell Plateaus and, of course, South America. Remarkably, the eastern boundaries of the southern subtropical gyres in all three basins apparently occur in the ocean interior, away from land. The Indian's subtropical gyre, and perhaps part of the South Atlantic's, reaches east to a retroflection just upstream of the Campbell Plateau south of New Zealand. Seasonal variability at 900 m is focused around the equator with weaker variability found near certain bathymetric features. There is a remarkable agreement between the observed seasonable variability and that predicted by the JPL-ECCO data-assimilating numerical model. Aside from seasonal effects, eddy variability is greatest along the equator, in tropical and subtropical western basins, and along the ACC. Integrals of velocity across regional passages (Tasman Sea, Mozambique Channel) provide useful reference for hydrographic analyses of transport. Across whole ocean basins, however, the uncertainty associated with the appropriate continuity relation for horizontal flow (e.g. geostrophy vs. non-divergence) is comparable to the mean flow.

1. Introduction

Less than 50 years after John Swallow (1955) announced the first neutrally buoyant subsurface float, the World Ocean Circulation Experiment (WOCE) set out to measure and map flow near 1000 m depth over the global ocean using floats. Assets were concentrated on a single level to produce an accurately measured level of known motion that could be used to reference the combination of historical and WOCE hydrographic data that provide extensive geostrophic shear measurements. Ultimately the geostrophic shear measurements and direct measurements of velocity should be combined to form a three-dimensional map of the general circulation.

Many WOCE float measurements were made using autonomous floats that are not acoustically tracked, but rather surface at regular intervals to be located by, and relay data to, System Argos satellites. While sacrificing knowledge of velocity variability between the surfacing intervals and losing the quasi-Lagrangian behavior provided by acoustically tracked floats, autonomous floats are long-lived and inexpensive enough to make it feasible to gather the long records needed to accurately map mean circulation on basin scales. Several regional analyses of intermediate-depth flow, based on both acoustic and autonomous floats, have appeared: Owens' (1991) analysis of pre-WOCE SOFAR floats in the northwestern Atlantic; analyses of autonomous floats in the South Pacific by Davis (1998), and of RAFOS floats in the North Pacific by Riser (2004); regional analyses in the South Atlantic by Boebel et al. (1999, 2003), Ollitrault (1999), and by Richardson and Garzoli (2003); and circulation maps of the Subpolar North Atlantic by Lavender et al. (2000, 2004) and Bower et al. (2002).

Mainly between 1991 and 1995, some 306 autonomous floats, mostly of the ALACE type (cf. Davis et al., 1991) were deployed in the equatorial and South Pacific, including the Pacific sector of the Southern Ocean. All but 23 of those floats had expired by July 2003 and it is time to update the analysis of early data by Davis (1998). Between 1994 and 1996, another 228 ALACE floats were deployed in the Indian Ocean, including its Southern Ocean sector. Only 90 of those floats were still operating at the end of 2003. The purpose of this paper is to report on the mean circulation, seasonal changes and eddy variability in intermediate-depth flow in the Indian and South Pacific Oceans seen by these floats. Integration of float results with hydrographic data is not attempted here. Apparently Wijffels et al.'s (2002) analysis of 32^{o}S in the Pacific is the only such integration yet completed.

Because ocean variability is generally more energetic than the mean flow, extracting accurate mean from observations requires substantial averaging. Variance of particle velocity averaged over a time, *t*, long compared with the correlation time of Lagrangian velocity is $\sigma_{ij} = 2K_{ij}^{\infty}\, t^{-1}$ where K_{ij}^{∞} is the asymptotic large-time Taylor (1921) eddy diffusivity. The information compiled by Boning (1988) suggests that mid-depth *K* is generally between 10^3 and 10^4 m^2s^{-1} so that the average velocity over a one-year record will be uncertain by 5 to 15 mm s^{-1}. Thus, multi-year records are necessary to achieve useful accuracy and for floats this requires spatial averaging or filtering. Because filtering can dominate the results, particular attention is paid here to comparing results from different analyses. Three averaging methods are used to bring out the patterns of the general circulation and eddy variability: (1) simple area-time averages in which all observations in a volume of space-time are averaged (Section 3); (2) fitting the data in a volume of space-time to a few simple local functions of position (Section 4), which is somewhat more effective in separating spatial structure from temporal variability; and (3) a novel application of objective mapping that allows continuity equations and boundary conditions to be applied (Section 6).

2. The Data

The autonomous float data used here were derived from raw surface positions following the procedures in Davis (1998); the procedure and errors are summarized in Appendix A. Basically, velocities measured from displacements, typically over 25 days, are subject to random errors of O(2 mm s^{-1}) associated with untracked surface motion and biases of O(0.3 %) of the shear between the drift depth and the surface. The data available through June 2003 in the Pacific comprise 23,876 displacements spanning 1332 float-years south of 24°N. Most are autonomous floats from the SIO WOCE program, but Steve Riser provided 14 float-years of RAFOS float data while 179 float-years of data are from SIO deployments for the Consortium on the Ocean's Role in Climate (CORC) and the early Argo program. Through November 2003 there are available in the Indian Ocean 1251 float-years from 19,899 displacements from the WOCE program and South Atlantic deployments by CORC. The two float arrays are depicted in Figures 1 and 2.

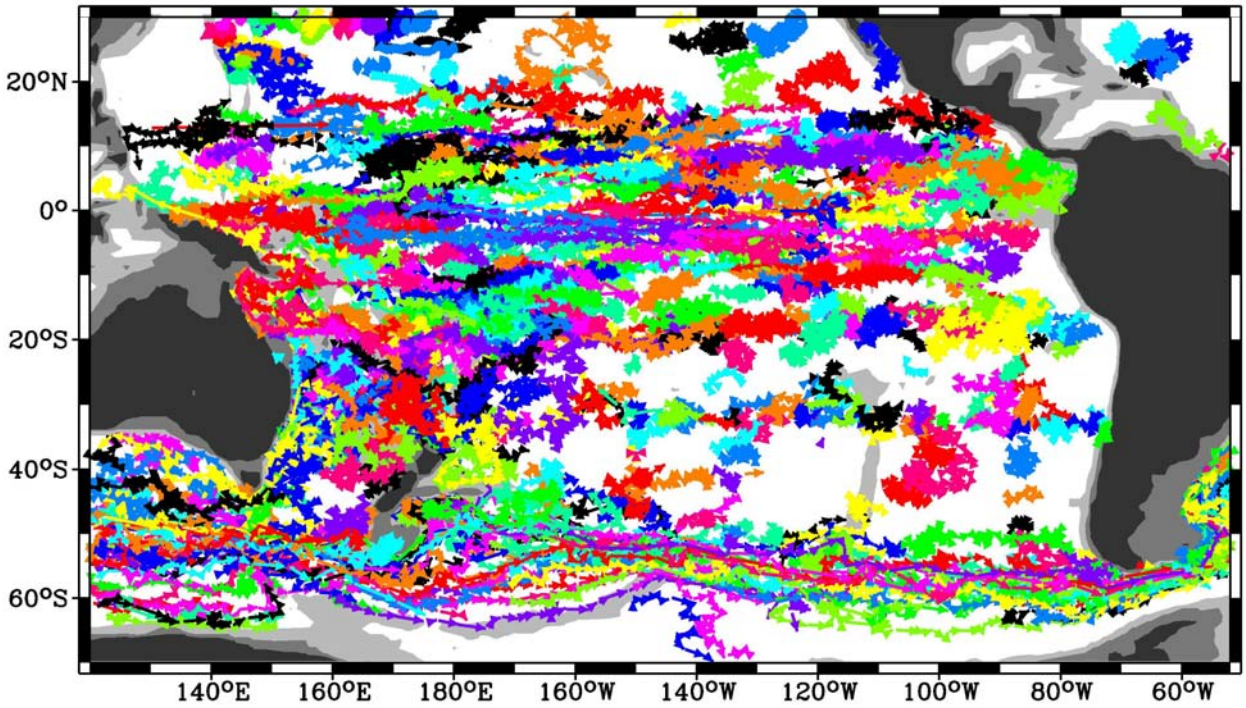

Figure 1. Float coverage in the Pacific. Each subsurface displacement (usually over 25 days) is shown as an arrow. All displacements from one float are in the same color. Depths less than 3000 m are shaded and those less than 700 m are shaded more darkly.

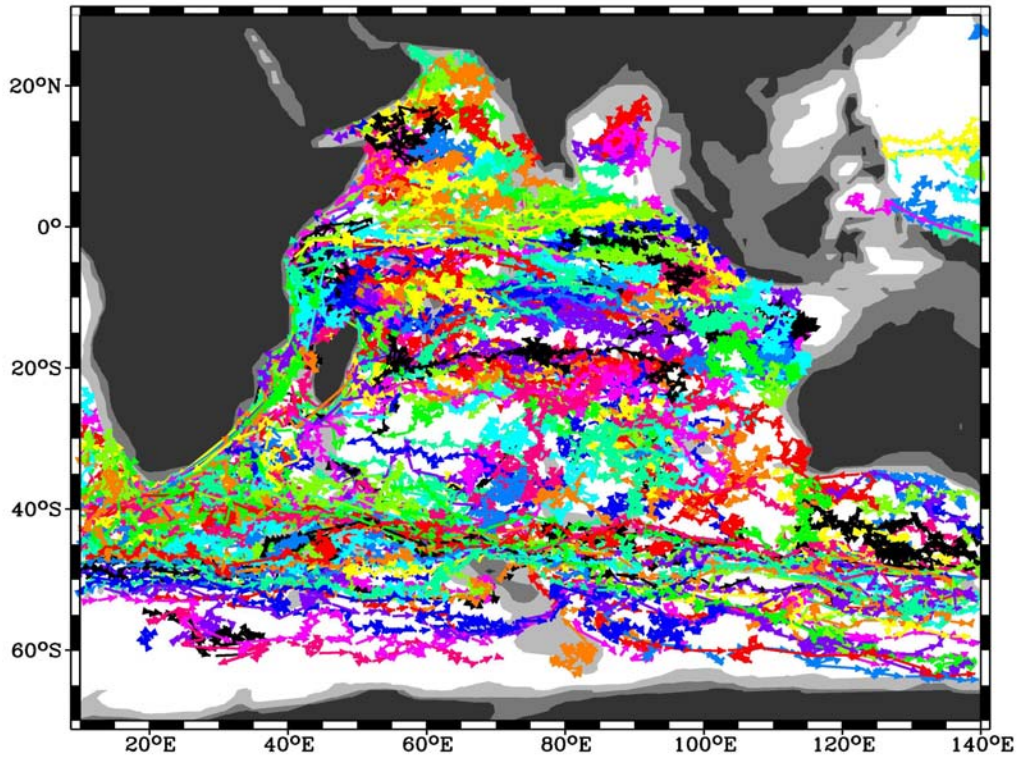

Figure 2. Float coverage in the Indian Ocean. Format is as in Figure 1.

While eddy noise and other variability makes interpretation of raw float tracks ambiguous, plots of unprocessed data describe the character of the data clearly and give some insight into the nature of regional circulations. Several such plots were included in the preliminary analysis of the South Pacific (Davis, 1998). Additional plots made possible by new data are presented here.

The more complete data now available clarifies the complex circulation around New Zealand, as shown in Figure 3. Davis (1998) showed that the complex flow patterns northeast of the North Island were similar to the mean pressure field found by Sutton and Roemmich (1998) from years of hydrographic data. The flow in Figure 3 is complex, but the raw trajectories mark out an intermediate-depth boundary current along the North Island's east coast flowing south and then eastward over the north flank of the Chatham Rise. South of this, there is a generally northward boundary flow north of Campbell Plateau that joins eastward flow along Chatham Rise. West of New Zealand, the flow appears confused.

The data in Davis (1998) showed a net flow to the northeast into the Coral Sea even though bathymetry blocks any flow out of the Sea in that direction. This appeared to be an artifact of a limited observational duration over which floats had entered the Coral Sea from the east but had not had time to depart. The more complete data in Figure 4 shows a cyclonic boundary current around the Coral Sea, fed by westward flow near 17^{o}S and exiting into the Solomon Sea. Floats exit the Solomon Sea by three distinct routes but are too few to define the dominant path. East of the Solomon Islands, mean flow is generally to the northwest toward the equator.

Three main features are evident in raw data from the Indian Ocean: an intermediate depth Agulhas Current, flow around the Madagascar, and a short intermediate-depth Somali Current flowing northward along the African coast between the equator and 6^{o}N. In other regions, general patterns of circulation are masked by eddy variability and some form of averaging is needed to define patterns of general circulation.

Figure 5 depicts raw data around Madagascar including counter flow boundary currents in the Mozambique Channel and a boundary current along the east coast of most of Madagascar that feeds the Agulhas Current. Chapman et al. (2003) examined these flows in detail. Figure 6 shows the strongest flow observed in the Indian Ocean, the intermediate-depth Agulhas Current, with peak velocities over 25 days exceed 50 cm s^{-1} in several cases. Perhaps more remarkable is the rapidity with which the flow accelerates near 29^{o}S and then decelerates near 37^{o}S after having passed the tip

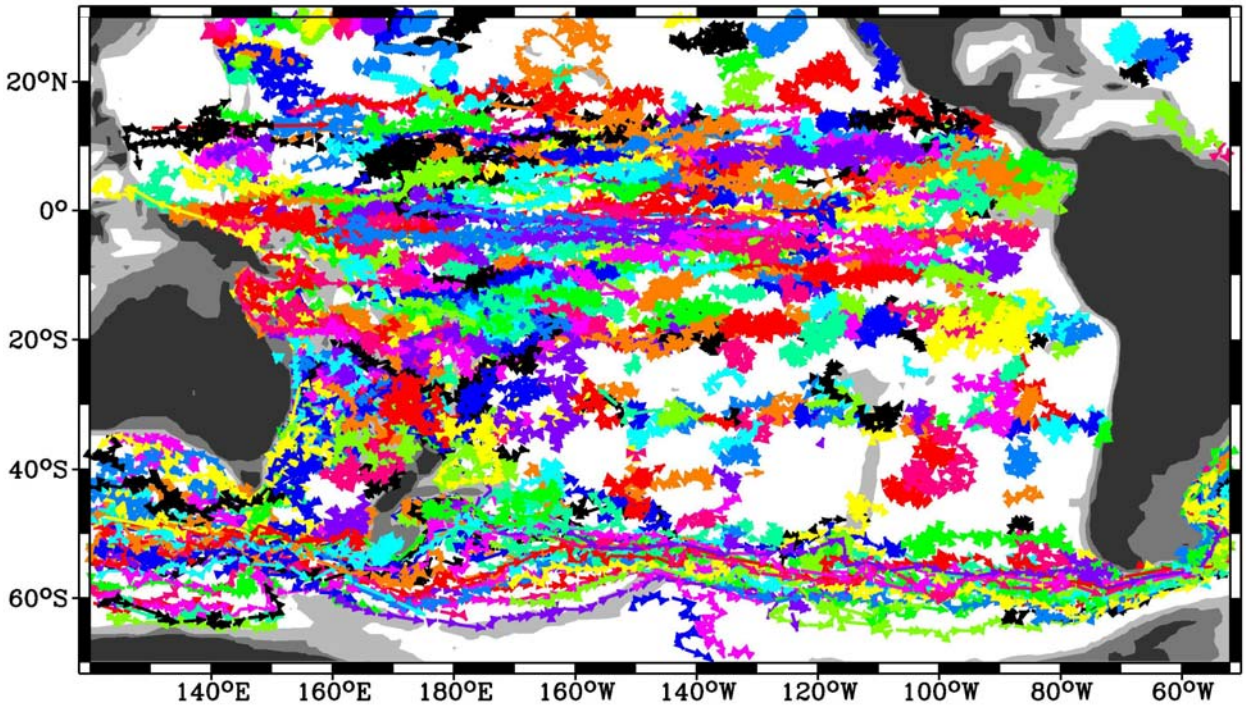

Figure 1. Float coverage in the Pacific. Each subsurface displacement (usually over 25 days) is shown as an arrow. All displacements from one float are in the same color. Depths less than 3000 m are shaded and those less than 700 m are shaded more darkly.

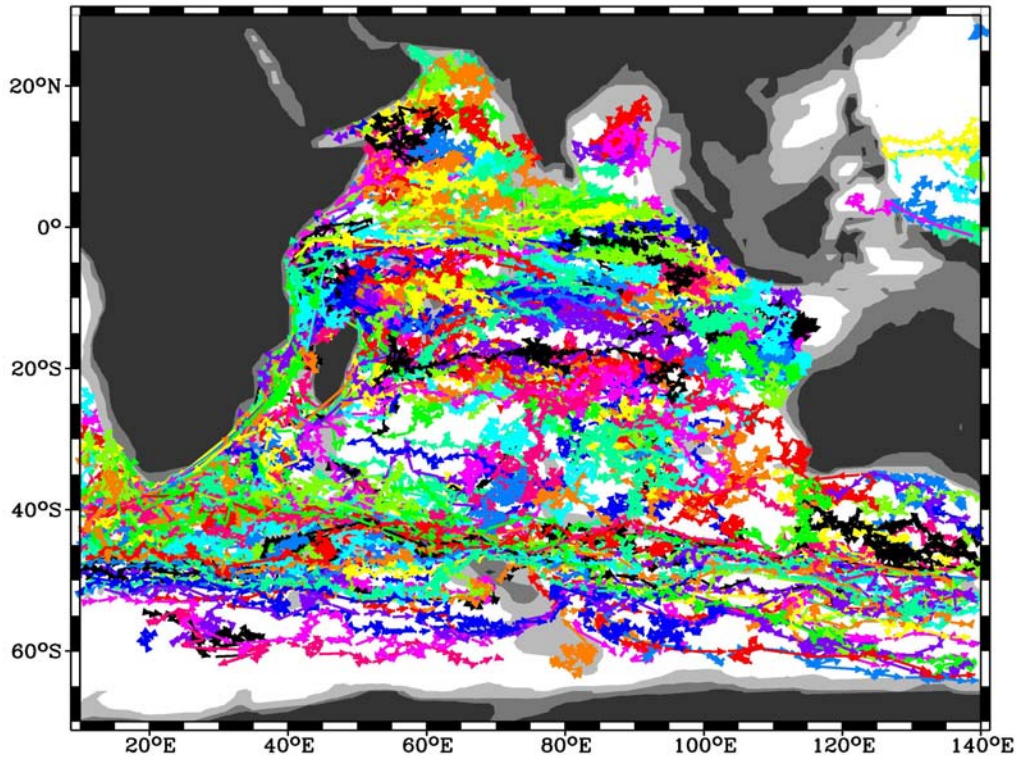

Figure 2. Float coverage in the Indian Ocean. Format is as in Figure 1.

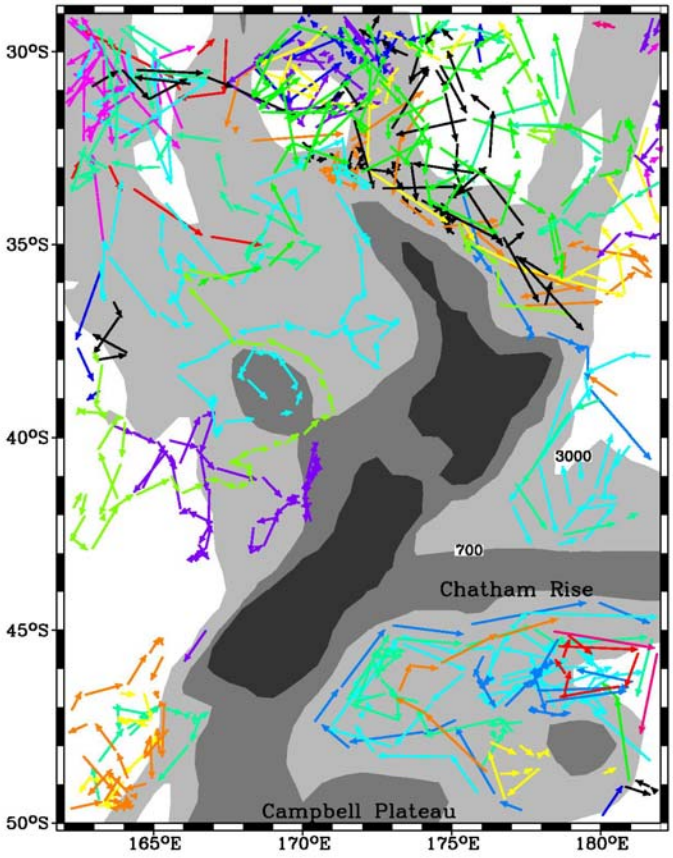

Figure 3. Raw subsurface float displacements (arrows) near New Zealand. Most displacements are over 25 day intervals near 900 m depth. All displacements from a float are in the same color. Land and depths less than 700 and 3000 m are shaded. Features are (a) southward flow along the North Island toward Chatham Rise in an intermediate-depth analog of the East Auckland Current, (b) westward flow north of Campbell Plateau that turns eastward along Chatham Rise, and (c) confused flow west of New Zealand. One float (cyan) is captured by and grounded on an eddy over the Lord Howe Rise (39°S, 169°E) while another (magenta) becomes grounded southeast of this feature.

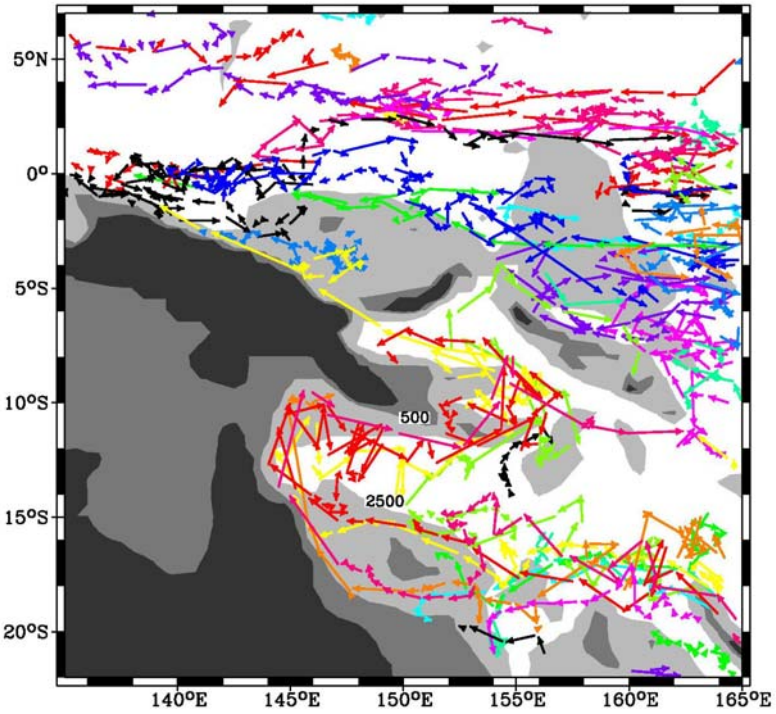

Figure 4. Raw trajectories around the Coral Sea and New Guinea in the format of Fig. 3. Flow enters the Coral Sea near 17°S, follows the western boundary around the Coral Sea and tip of New Guinea. One float (yellow) travels north-westward at speeds over 15 cm s^{-1} along the New Guinea coast while others escape the Solomon Sea to the east and through the Solomon Islands. Flow is toward the equator east of the Solomon Islands. Equatorial flow is zonal but in both directions, so the sense of mean flow cannot be determined without averaging.

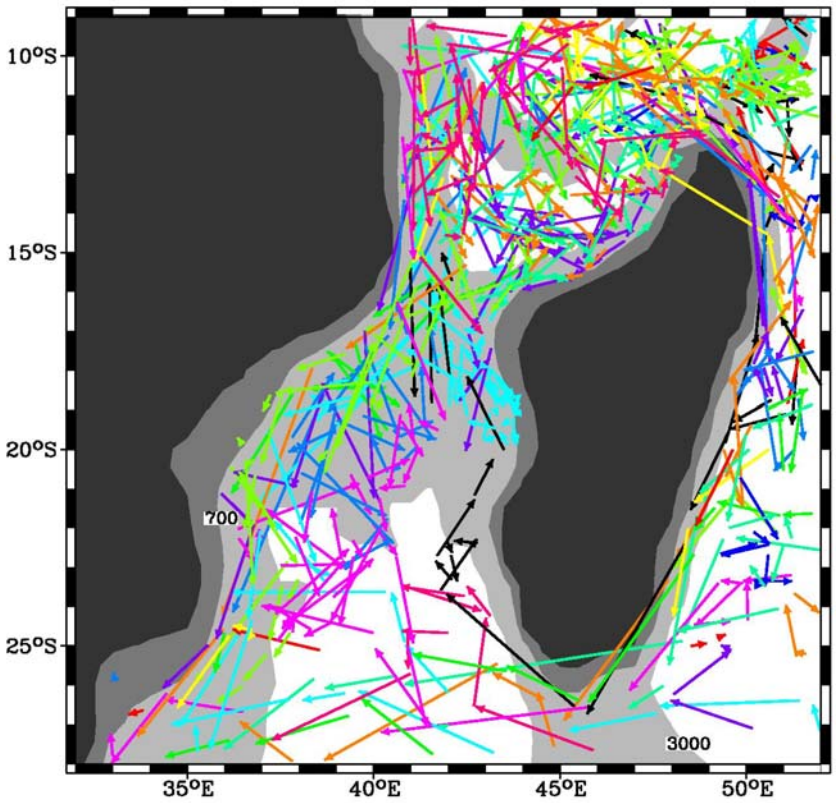

Figure 5. Raw data near Madagascar. Note (a) a bifurcation on the east coast of Madagascar that feeds a southward boundary current, which feeds the Agulhas and a northward flowing eastern boundary current in the Mozambique Channel, (b) a flow north from the bifurcation that then flows west to Africa, (c) a southward boundary current along the African coast, including Mozambique Channel, and (d) an anti-cyclonic eddy in the northern Channel encompassing the southward boundary current along Africa and the northward boundary current along the west coast of Madagascar.

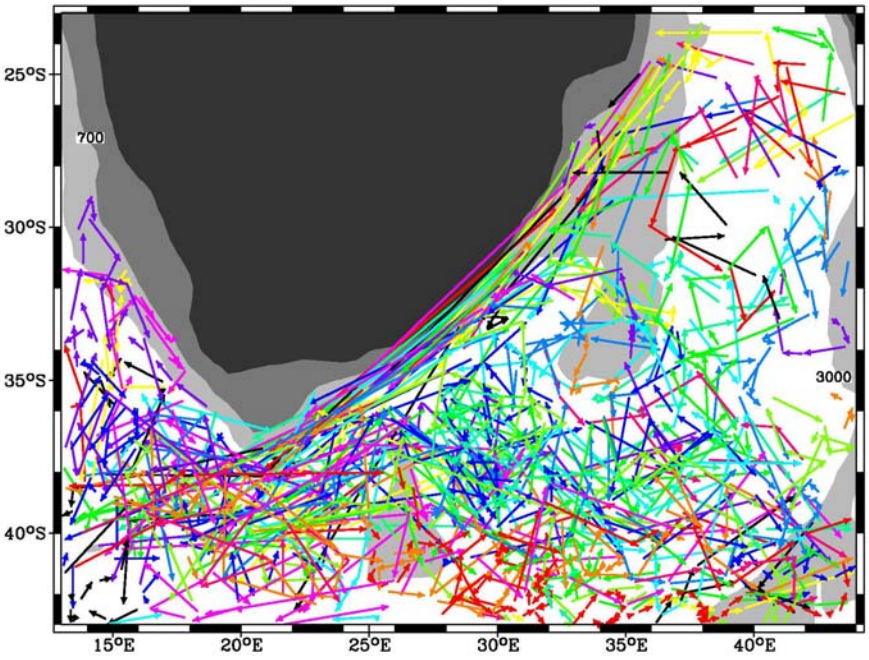

Figure 6. Raw displacements around South Africa. In the northeast corner of the figure is the flow south of Madagascar (Figure 5). Peak speeds in the intermediate-depth Agulhas Current exceed 50 cm s^{-1}. Note the rapidity with which this current accelerates and decelerates. The frequency of eastward flow along 40°S suggests a retroflection of this current while confused flow west of Africa suggests flow into the Atlantic.

of Africa. Several floats went from speeds of a few cm s^{-1} north of the Agulhas, passed through the boundary current in one or two submergence cycles of 25 days and, after clearing the tip of Africa, decelerated again to a few cm s^{-1} where the Agulhas encounters the eastward flowing South Atlantic Current and apparently breaks up into eddies. Although vigorous eddy motion clouds general patterns, the frequency of eastward displacements shows the Agulhas to feed an eastward retroflection as well as a confused flow into the Atlantic. There is no sign in the Agulhas region of the undercurrent described by Beal and Bryden (1999), perhaps because this current is confined very near the slope above 1000 m, because the current is transient (only present about half the time at 1189 m), or because it is part of a recirculation which floats cannot sample unless deployed in it.

3. Area Averages

The raw data in Figures 1-6 make clear that averaging is required to describe patterns of mean circulation in the face of ubiquitous eddy variability. Based on the quantity of data available and the rough sampling errors given in Section 1, it should be possible to map mean velocity over regions of O(500 km) dimension with accuracy near 2 mm s^{-1} in eddy quiet regions and O(7 mm s^{-1}) in eddy-rich boundary currents. This section presents the simplest mean-flow estimate, an average over all available observations in an area.

Because float displacements sometimes exceed 1000 km, it is necessary to treat each displacement as an integral of velocity along a trajectory. To do this, hypothetical trajectories connecting dive and surfacing positions are defined. If a displacement was less than 200-km, its velocity was assigned to the grid point closest to the displacement mid-point. Endpoints separated by more than 200 km were connected by a path on the one-degree grid that was the shortest path not crossing bathymetry shallower than 900 m. Each long path was then subdivided into segments of less than 200 km by M points x and the displacement was modeled as the finite-difference analog of an integral of velocity along its hypothetical trajectory:

$$\vec{d}(m) = \sum_{x}^{M} \vec{U}(x)\,\delta(x) + \vec{n}(m) \qquad \text{where} \qquad \delta(x) = t(m)/M\ , \tag{1}$$

$\vec{U}$ is the mean velocity field, $\vec{n}(m)$ is the eddy noise on the displacement, $t(m)$ is the duration of displacement m, and the sum is over the M points x in the "path" for displacement m. Grounded floats were excluded from all statistical analyses.

Seasonal Variability

Because the sampling arrays are sparse and irregular in time and space, it is important to remove coherently any seasonal cycle before averaging to find mean values. Davis (1998) showed that there is seasonal velocity variability in the tropical Pacific at 1 km depth and that the modes of seasonal variability in numerical models are effective basis functions for describing the observed seasonal variability. Dr. Benyang Tang of the Jet Propulsion Laboratory provided Empirical Orthogonal Functions (EOFs) of velocity from ten-year runs in the Indian and Pacific Oceans using the ECCO program's data assimilating ocean circulation model. The dominant EOFs (patterns of variability) from each ocean, shown in Figure 7, are focused within 10^o of the equator although signals are apparent south of Australia and in the Bay of Bengal. Zonal scales of the equatorial patterns are O(5000 km) and the meridional structure has flow at $\sim \pm 5^O$ latitude oppositely directed to that along the equator. The next most energetic EOFs in each basin have similar zonal scales but two additional flow reversals with latitude. Higher modes are more complex in both zonal and meridional structure.

The float velocity observations were fit to the first four EOFs in each basin by minimizing the squared data misfit normalized by the expected squared observational error, itself based on the record length and the diffusivity estimated below. The model did not assimilate any float data or any other intermediate-depth velocities and the EOF patterns were the only model information used. Even though the EOFs have complex structures and involve large variations over only a few hundred kilometers, and even though the wind forcing for the model may be in error, the observed and modeled seasonal cycles of EOF amplitudes are in remarkable agreement. Figure 8 shows the seasonal cycles of float and model amplitudes for the first three modes in each ocean. Contrasting the semi-annual period of the main variability in the Indian Ocean with the annual period in the Pacific suggests that local winds in the tropics are the main forcing of the intermediate-depth seasonal cycle. For all subsequent analyses the seasonal cycles, based on fitting data in each basin to 4 EOFs, were subtracted from the data.

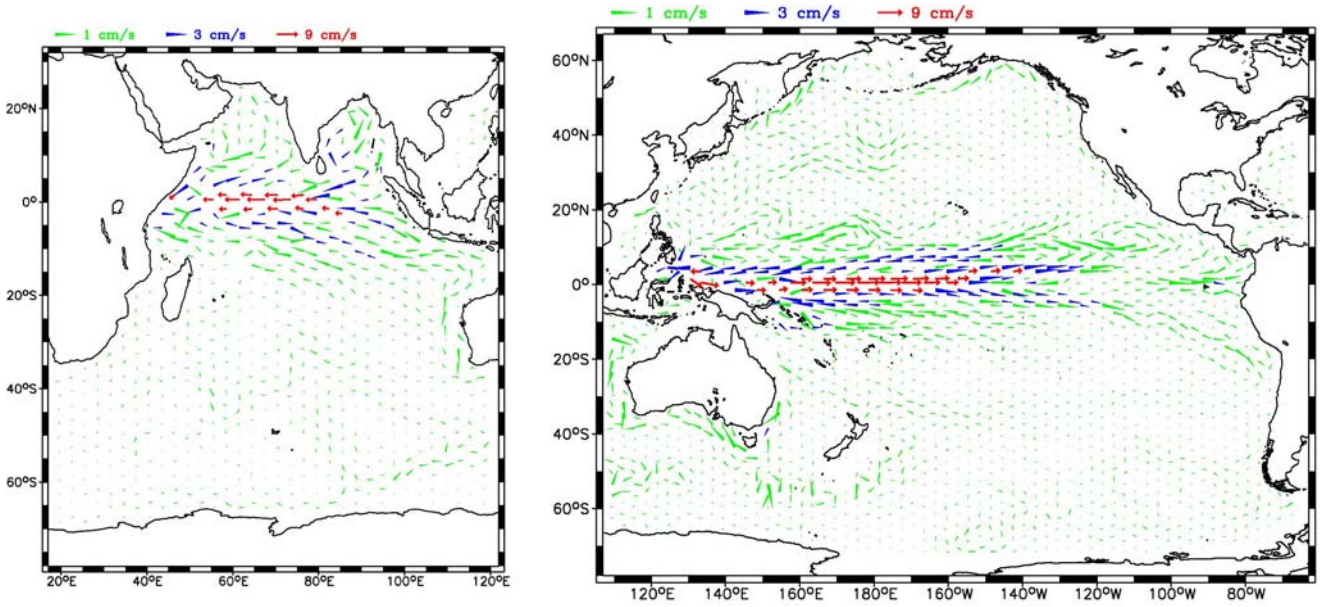

Figure 7. Velocity of the dominant EOFs for the Indian (left) and Pacific Oceans (right) from the JPL-ECCO data-assimilating numerical model (courtesy Dr. Benyang Tang). Each EOF is scaled so its speed equals the standard deviation of the velocity it explains. Velocities less than 1 cm/s are in green using the scale at the upper left. Speeds between 1 and 2 cm/s are in blue and above 2 cm/s is in red.

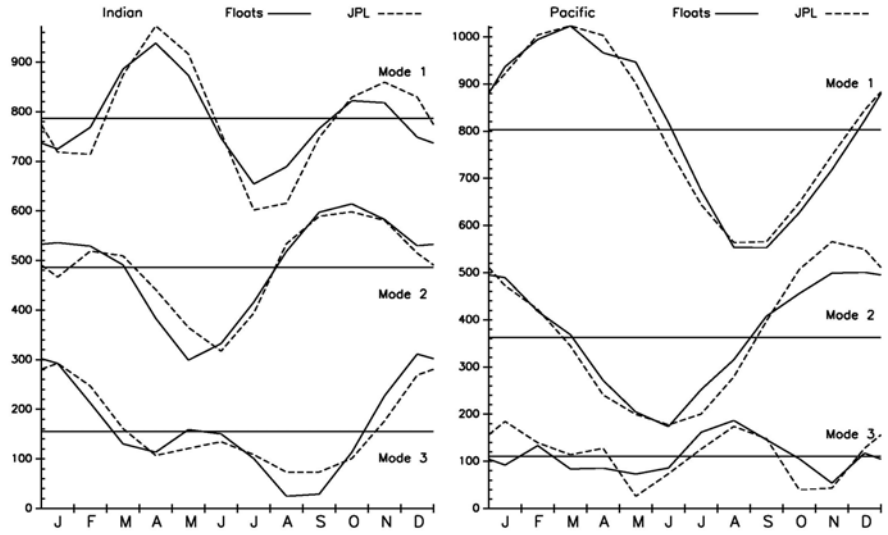

Figure 8. Seasonal cycle of EOF amplitudes for the Indian (left) and Pacific Oceans (right). Solid lines are the amplitudes of the first three most energetic EOFs when fit to float velocities. Dashed lines are the amplitudes of these modes in the JPL/ECCO data-assimilating model.

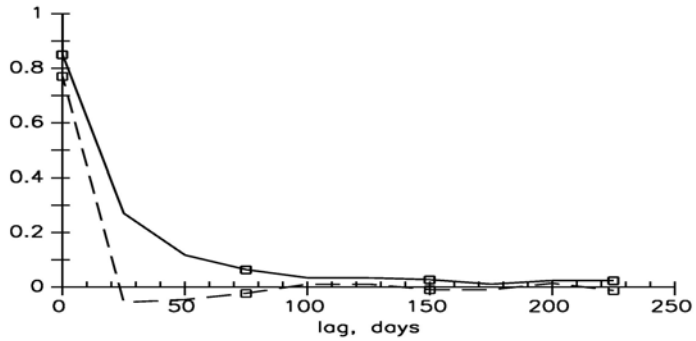

Figure 9. Lagrangian time-lagged correlation of east velocity *u* (solid) and *v* (dashed). Bins are 25 days. The zero-lag bin includes some non-zero-lag pairs. Data from the Indian and South Pacific Oceans is combined. Area-average mean velocities (Figs. 10 and 11) were removed, as were the 4-EOF annual cycles in each ocean.

Mean Circulation

Area averages include data from all trajectory points within a specified "distance" of a grid point. Because bathymetry causes flow to have longer scales along depth contours than across them, the distance between points *r* includes a factor that increases the distance between points if their water depths differ:

$$r = \sqrt{r_{GEO}^2 + \mu^2 \ln^2(\frac{H_1}{H_2})} \qquad (2)$$

where r_{GEO} is the geographical distance, H_1 and H_2 are the water depths at the two points, and μ is a parameter controlling the water-change penalty. At each grid point all data (i.e., points along the paths) with $r < r_{MAX}$ were included in the average. The r_{MAX} for each average was adjusted to make all averaging areas equal to πR_{AV}^2. To minimize error, velocities falling in $r < R_{MAX}$ were averaged with weighting inversely proportional to the sampling-error standard deviation based on each displacement being independent.

When the spatial mean velocity (Figures 10 and 11) is subtracted from observations but no account is made for the seasonal cycle, the Lagrangian time-lagged correlation depends strongly on latitude in both basins with low latitudes having longer time scales than higher-latitude regions. If the seasonal cycle subtracted, the Lagrangian time-lagged structure does not depend significantly on latitude and can be characterized by single curves for eastward and northward velocities *u* and *v* (Figure 9). The correlation of *v* effectively vanishes for lags of 25 days or longer whereas the decorrelation time of *u* is about 75 days. Presumably the anisotropy is a consequence of the variation of the Coriolis parameter; it is more apparent in the Pacific than in the Indian Ocean. The transverse isotropic Lagrangian correlation of nearly simultaneous velocities (not shown) vanishes in 50 km and the longitudinal correlation nearly vanishes for lags greater than 100 km. Because observations within 100 km are rare and the sequential correlation of velocities is weak, all observations in an area average are treated as independent.

The sampling variance of displacements over differing durations, *t*, was assumed to grow linearly with time *t* according to Taylor's (1921) asymptotic law

$$< d_i'(t)\, d_j'(t) > = \int_0^t ds\, [K_{ij}(s) + K_{ji}(s)] \xrightarrow[t\to\infty]{} 2\, K_{ij}^{\infty}\, t \qquad (3)$$

where $K(t)$ is the Taylor diffusivity that approaches the asymptote K^{∞} when *t* greatly exceeds the Lagrangian decorrelation time. This asymptotic relation is used to weight the data in area averages, to estimate the uncertainty of the average, and to estimate the diffusivity. When the variance of velocity measured over duration *t* is 2*K/t*, the minimum-square-error average from an ensemble of independent velocity observations is the sum of the displacements divided by the sum of the durations and this weighting is used here.

Figures 10 and 11 show the area-average mean flow computed for the Indian and Pacific Oceans, respectively. Sampling error (not shown) is of O(5 mm s^{-1}) in both basins so that vectors (plotted in green) with |**u**| < 1 cm s^{-1} are not individually significant. Velocities with |**u**| > 3 cm s^{-1} (plotted in red) are generally very accurately known with uncertainty substantially smaller than the mean velocity. Figure 10 updates the analogous preliminary plot in Davis (1998); there remain several areas where there are too few data to compute averages, particularly in the eastern subtropical South Pacific where flow is too weak to fill holes in the deployment array. The Indian Ocean area average flow in Figure 11 is the first directly measured circulation of intermediate-depth flow in the Indian Ocean; coverage is generally better than in the Pacific although the Bay of Bengal is poorly covered. Sampling errors are similar to those shown below for fitting data to local functions. The intermediate flow includes the main elements found in the near-surface circulation and is discussed below.

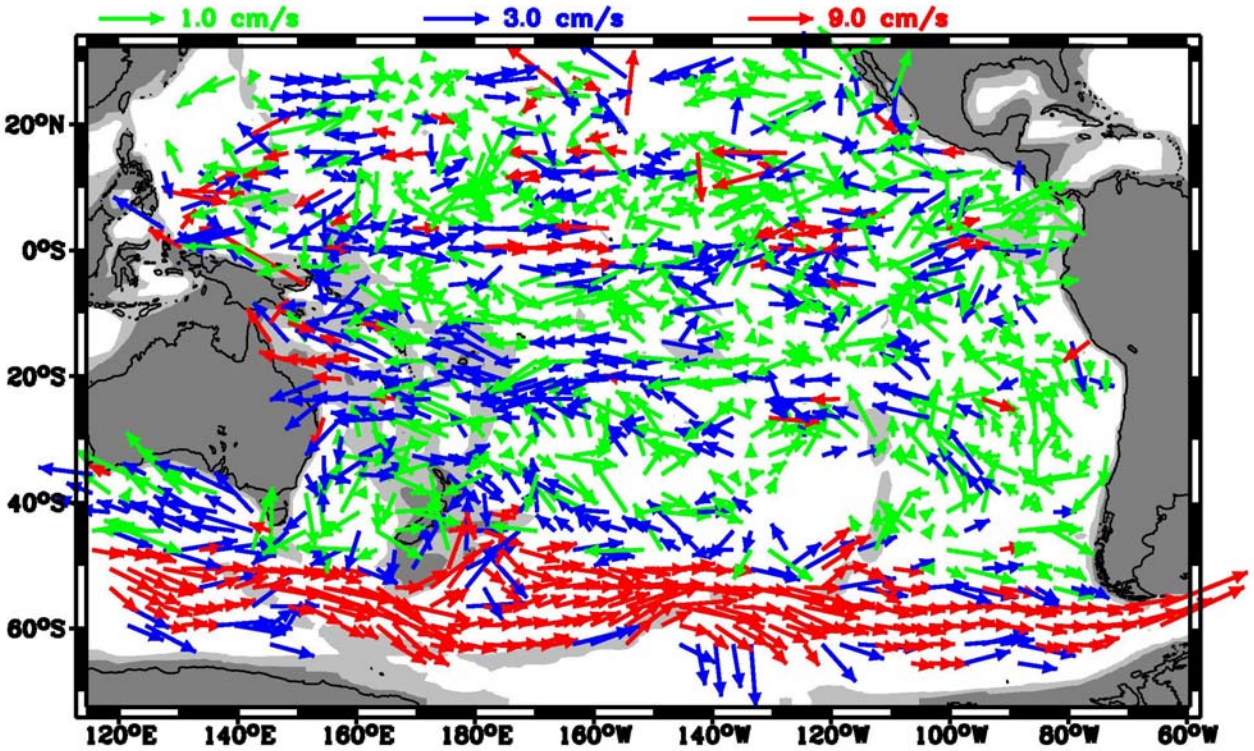

Figure 10. Area-average mean velocity at 900 m in the Pacific Ocean from 1332 float-years of data using parameters R_{AV} = 300 km and μ =300 km. Arrows show speed and direction at the arrow's base on a nominal 3° grid. Speeds $|\mathbf{u}| < 1$ cm s^{-1} are plotted in green using the green scale at the top. Blue is for 1 cm s^{-1} < $|\mathbf{u}|$ < 3 cm s^{-1}. Red is used when $|\mathbf{u}| > 3$ cm s^{-1}. Shading denotes the 900 m and 3000 m isobaths in the bathymetry, smoothed to one-degree resolution, used in shaping the averaging cells.

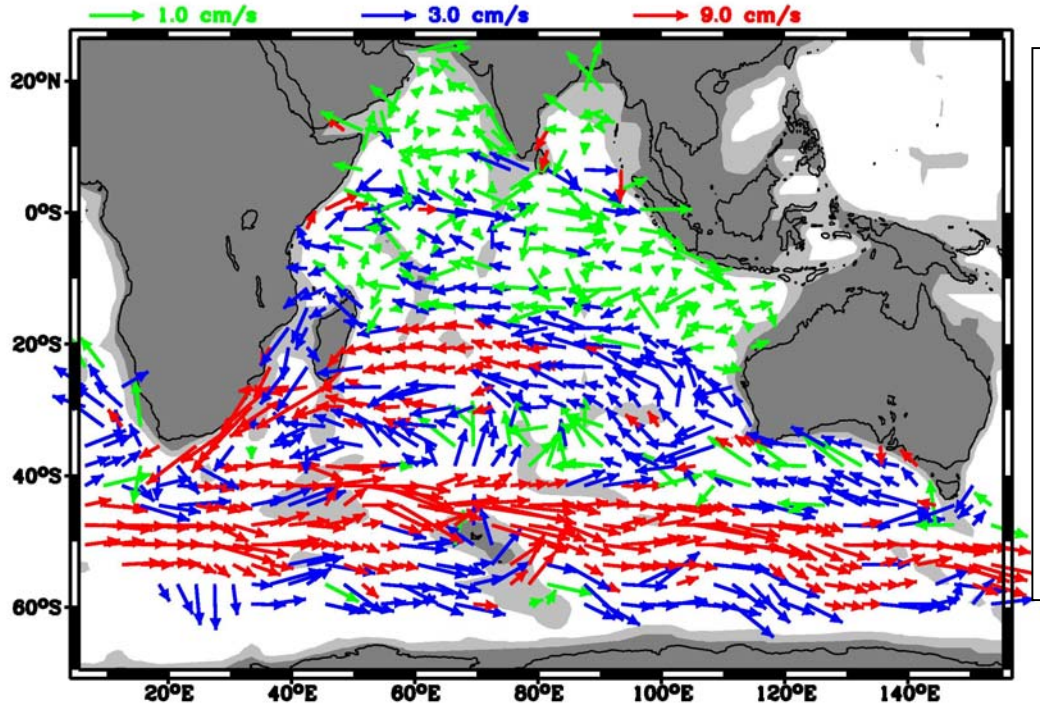

Figure 11. Area-average mean flow at 900 m in the Indian deduced from 1291 float-years of data using parameters R_{AV} =300 km and μ =300 km. Format is as in Figure 10.

4. Local Function Fitting

Area averaging has the great advantage of transparent simplicity, but the procedure is clumsy. In the presence of sheared mean, it confuses time variability and mean shear. A somewhat more effective, if less transparent, way to filter variability from observations is to fit all the observations in a small region to a few functions representing a mean current and linear mean shear. These local fits then specify velocity on a regular grid that extends into small data voids. Eddy variability based on this mean is more reliable because it is not inflated by the effects of mean shear, as it is in area-averages.

Data were fit to five nondivergent velocity functions

$$\mathbf{U}(\mathbf{x}) = a_1\hat{\mathbf{x}} + a_2\hat{\mathbf{y}} + a_3\,\hat{\mathbf{x}}\,(y-y_0) + a_4\,\hat{\mathbf{y}}\,(x-x_0) + a_5\,[\,\hat{\mathbf{x}}\,(x-x_0) + \hat{\mathbf{y}}\,(y-y_0)\,] = \mathbf{F}\,\mathbf{a} \qquad (4)$$

where $\hat{\mathbf{x}}$ and $\hat{\mathbf{y}}$ are eastward and northward unit vectors and $\mathbf{x}_0$ is the center of the averaging area. All the data **d** within a radius R_{FIT} of the point $\mathbf{x}_0$ were used to determine the amplitudes **a** by simultaneously minimizing data misfit and the size of |**a**|. Specifically, **a** minimizes

$$Q = (\mathbf{d} - \mathbf{H}\mathbf{F}\mathbf{a})^{\mathrm{T}}\,\mathbf{E}^{-1}(\mathbf{d} - \mathbf{H}\mathbf{F}\mathbf{a}) + \mathbf{a}^{\mathrm{T}}\mathbf{A}^{-1}\mathbf{a}\,, \qquad (5)$$

where **H** is the sampling matrix that connects the velocity field **u** to the data **d** (like the δ s in (1)), **E** is the covariance of **d**, and **A** is the amplitude mean product $< \mathbf{a}\mathbf{a}^{\mathrm{T}} >$. Here **A** and **E** were taken as diagonal with $A_{11}=A_{22}=10$ cm^2 s^{-2}, $A_{33}=A_{44}=0.01$ cm^2 s^{-2} km^{-2}, $A_{55}=0.0025$ cm^2 s^{-2} km^{-2} and **E** estimated from (3) using diffusivities from area averaging. The resulting circulations in Figures 12 and 13 are similar to the area averages in Figures 10 and 11. The function-fit fields have fewer gaps and, for $R_{AV} = R_{FIT}$, are smoother. The difference between methods is greater in the Pacific, where sampling density is lower and there are more significant data voids.

Figure 12 describes the major components of the Pacific's circulation including the abbreviations used here. Although smoother than the area-average result (Figure 10), the major features are little changed and not smeared out. As found by Kamenkovitch (1962), Gordon et al. (1978) and Gille (2003), bathymetry steers the ACC/SPC around the Campbell Plateau south of New Zealand and over the Pacific-Antarctic Ridge near 140^{o}W. The main departures from this current are toward the eastern Ross Sea near 135^{o}W, a retroflection into westward flow south of

Australia, and flow into the subtropical gyre near 115^{o}W over the East Pacific Rise. The western limb of the subtropical gyre includes a strong EAC between 20^{o}S and 35^{o}S; some of this flow crosses the Tasman Sea passing northeast of New Zealand and joins the SPC over the Chatham Rise (see also Fig. 3) while some continues south and flows past Tasmania. The eastern limb of the subtropical gyre is apparently focused near 100^{o}W, well offshore of South America (although there is little data to the east of this, the existing data precludes an significant flow to the north or west out of this under-measured region). The SEC and eastward equatorial flow form a tropical gyre closed in the west by a boundary current along the Great Barrier that passes through the Coral Sea and east of New Guinea. The eastern branch of this tropical gyre is confused. The northern tropical gyre involves the NEC and apparently crosses the entire basin near 10^{o}N. The eastern limb of the northern tropical gyre, like its southern counterpart, is confused, as is the source of the NEC. More properly part of the Indian Ocean circulation, the intermediate-depth Tasman Current south of Australia is fed by the weak southern EAC and by retroflection of the ACC (or South Indian Current) in an uncertain ratio.

The Indian Ocean circulation (Figure 13, where abbreviations for the main currents are introduced) is dominated by eastward flow centered between 40^{o}S and 55^{o}S comprising the ACC and SIC. Speeds are typically 5-10 cm s^{-1} across a ~10^{o} width and the path is fairly straight except for a slight northward perturbation around Kerguelen Ridge at 70^{o}E. A well-developed SEC, with speeds of 2-5 cm s^{-1}, feeds southward flow around both sides of Madagascar and ultimately a narrow and strong intermediate depth Agulhas Current. Speeds of the mean in the Agulhas are strong (10-20 cm s^{-1}) and the acceleration/deceleration is remarkable with mean velocity doubling and then halving in just a few days following a fluid parcel (see Fig. 6 for details).

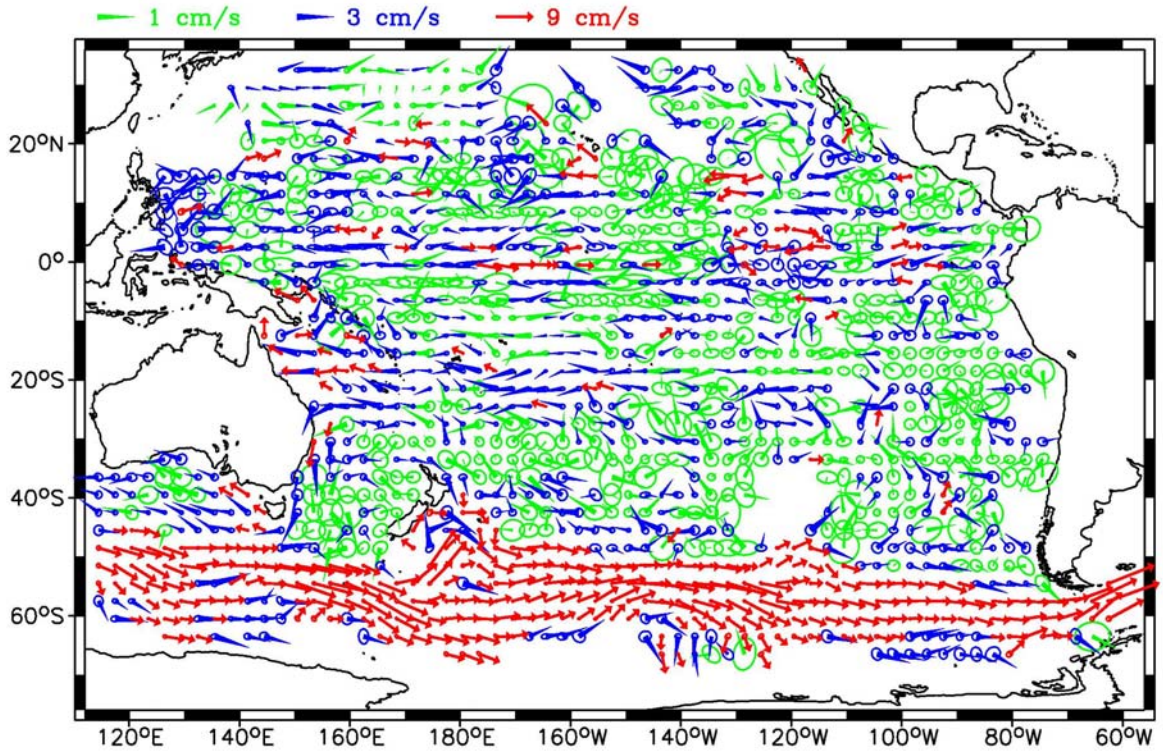

Figure 12. Mean velocity vectors with sampling error ellipses at their base for 900 m depth in the Pacific calculated by fitting to 5 functions of constant or linearly sheared nondivergent velocity over an area with radius R_{FIT} = 300 km. Three color-coded scales are used: green for mean speed $q < 1$ cm s^{-1}; blue for $1 < q < 3$ cm s^{-1}; red for $q > 3$ cm s^{-1}. From north to south, the elements of the circulation are (a) in the western Pacific north of 20°N, an eastward flow of O(1 cm s^{-1}) that apparently receives flow from the intermediate-depth North Equatorial Current (NEC); (b) a westward NEC west of 140°W along 10°N; (c) a generally eastward flow along the equator apparently fed from the equatorward flow east of New Guinea; (d) a westward intermediate depth South equatorial Current (SEC) that crosses the basin at 20°S in the east and 20°S in the west; (e) flow from the SEC northwestward into the Coral Sea to feed the equatorward flow past New Guinea and southward along Australia in an intermediate depth East Australia Current (EAC); (f) eastward flow from the EAC past the north of New Zealand and then southeastward to join the strong eastward flow south of 50°S; (g) a strong eastward flow between 50°S and 60°S that comprises the Antarctic Circumpolar Current (ACC) and the poleward branch of the subtropical gyre, the South Pacific Current (SPC); (h) the northward flowing eastern branch of the subtropical gyre centered near 100°W; (i) westward current south of Australia apparently partly fed by the EAC but mainly from retroflection of the eastward flow to the south, which Figure 13 indicates is the eastern limb of the Indian Ocean's subtropical gyre; and (j) a flow south from the ACC toward the eastern Ross Sea near 135°W .

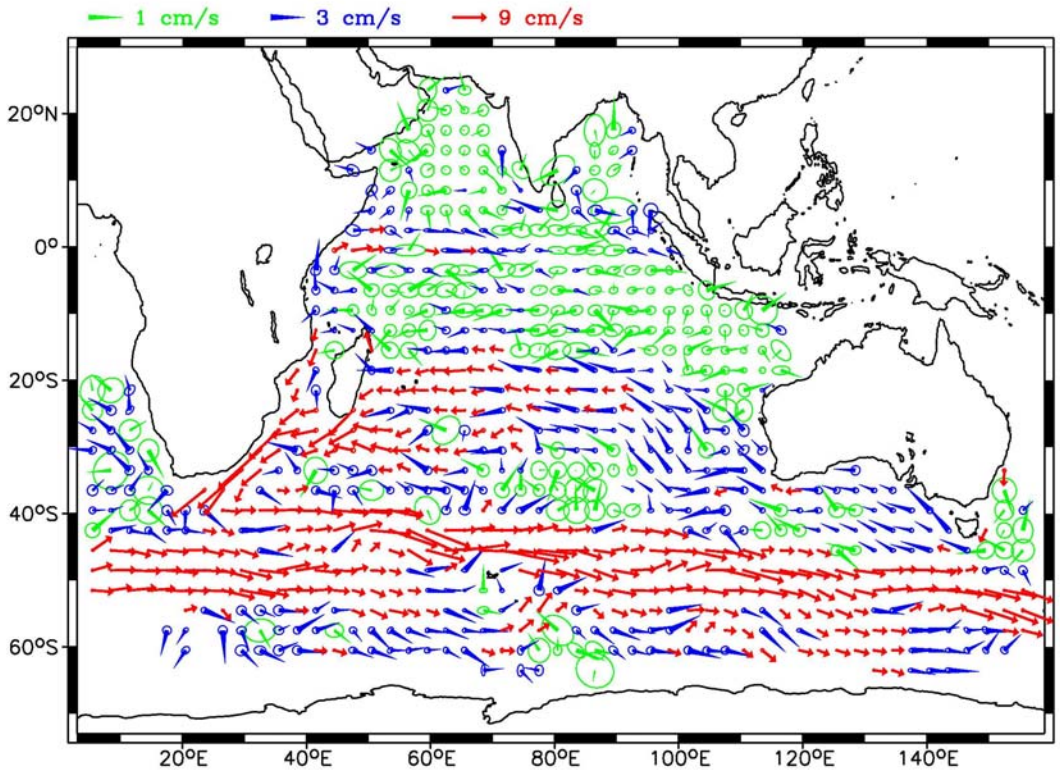

Figure 13. Mean flow and error ellipses for the Indian Ocean at 900 m in the format of Fig. 12. Flow north of the equator is confused except for westward flow out of the Bay of Bengal and past the tip of India and trans-equatorial flow in the eastern equatorial zone that appears to feed a weak but distinct southeastward flowing boundary current along the Indonesian Archipelago. This boundary current is the eastern limb of a tropical gyre that includes a westward South Equatorial Current (SEC), an intermediate-depth Somalia Current along Africa, and eastward flow along the equator. There is no evidence of the Great Whorl in the Arabian Sea. Most of the SEC feeds the subtropical gyre through southwestward flow east of Madagascar and a smaller flow north of Madagascar that then passes southward through the western Mozambique Channel. Both sources feed an intermediate-depth Agulhas Current that accelerates to speeds over 20 cm s^{-1}. Most of the Agulhas retroflects to the east along 40°S to form a South Indian Current (SIC) that appears to be distinct from the ACC west of 80°E. The eastern limb of the subtropical gyre may extend as far as 145°E before turning back to feed the Tasman Current south of Australia. This westward flow might be regarded as the SEC displaced south of its equilibrium by the continent that is also fed from the EAC and thus represent an inter-basin flow. Passing Australia the SEC drifts equatorward to 20°S where it impinges on Madagascar. It is difficult to separate possible flow through Indonesian Seas from the eastern parts of the tropical and subtropical gyres. Similarly, east of Africa it is difficult to tell how much of the northwestward flow is an inter-basin flow from the Agulhas.

5. Eddy Variability

While autonomous floats are well suited for gathering the long records required to establish mean flows, the interruption of Lagrangian trajectories at each surfacing makes them less well suited to describing eddy variability. The covariance of the eddy component of the submerged velocities (most over 25 days) is easily reported but these are hard to compare with instantaneous velocity covariance without knowing the Lagrangian frequency spectrum. It would perhaps be more meaningful to report the asymptotic single particle diffusivity K^{∞} of (3) but surface interruptions corrupt the long-time behavior required for this.

Here, diffusivity is calculated from displacement anomalies $\mathbf{d}'$ based on submerged displacements **d** minus the displacement <**d**> a particle would experience following the mean flow for the same time interval. Within our approximation for the path, <**d**> is the displacement computed from the mean velocity as

$$\overline{\mathbf{U}} = \frac{1}{N}\sum_{n}^{N} \mathbf{U}(\mathbf{x_n}) \tag{6}$$

where **U** is the mean velocity from function fitting and the $\mathbf{x}_n$ are the N points along the approximate path. While the mean velocity from local function fitting is not dramatically superior to its area averaging equivalent, the diffusivity estimate is more robust and accurate because fitting is more efficient at separating temporal variability from mean shear. The reported diffusivity is

$$K_{ij} = < d_i' d_j' / 2t > \tag{7}$$

where each float displacement contributes one diffusivity estimate, $d_i' d_j' / 2t$, to the average.

Diffusivities have been estimated from pseudo-Lagrangian data in many different ways ranging from multiplying measured instantaneous velocity variance by an assumed integral time scale to integrating the time-lagged Lagrangian velocity covariance to some finite lag. Any such estimate is imperfect because K^{∞} is the infinite integral of the velocity covariance (equivalent to the zero-frequency limit of the Lagrangian frequency spectrum) and any estimate based on finite time lags is problematic. Subsurface measurements often, but not always, show dispersion $< d'(t)d'(t) >$ to grow roughly as the duration t after O(10 days). K of (7) equals K^{∞} only if the dispersion vs. duration curve at 25 days falls on the large-t asymptote. Dispersion vs. duration

curves shown by Freeland et al. (1975), Rossby et al. (1983), Figueroa and Olson (1989), and others suggest that the estimate (7) is typically high, usually by a factor less than 2. Because autonomous float trajectories are interrupted by an on-surface interval, we have not employed any method for estimating diffusivities that involves displacements over multiple submergence cycles. The covariance of the 25-day displacement-averaged velocity is equal to the reported diffusivity divided by 12.5 days.

Figures 14 and 15 show the 900-m lateral eddy-diffusivities for the Pacific and Indian Oceans, respectively. Eddy variability is significantly stronger in the Indian Ocean, particularly in the western basin where the largest diffusivities are found in the Agulhas, but even the diffusivities in low-energy regions are significantly larger than values in the analogous parts of the Pacific. In both oceans, eddy variability is generally strongest in the regions of strong mean flow and in a strip along the equator. Variability is reasonably isotropic everywhere except along the equator and at the tip of Africa where the Agulhas retroflects. In the Agulhas, the polarization of anomalous velocities suggests that they are partly residuals from excess smoothing associated with estimating the mean flow. The diffusivity is approximately isotropic in all other regions except the equator.

Dramatic geographic variability precludes meaningful comparison of diffusivities with those measured by others. It suffices to say that they are in the range of magnitudes for intermediate-depths described by Boning (1988) and that the range of spatial variation is even greater than that described by Lavender et al. (2003) in the North Atlantic. The diffusivity is generally larger than typical in the results from these, and other, sources. This may reflect expected bias associated with the assumption that dispersion has reached its large-t asymptote in 25 days or it may indicate lower eddy activity in the regions studied by others.

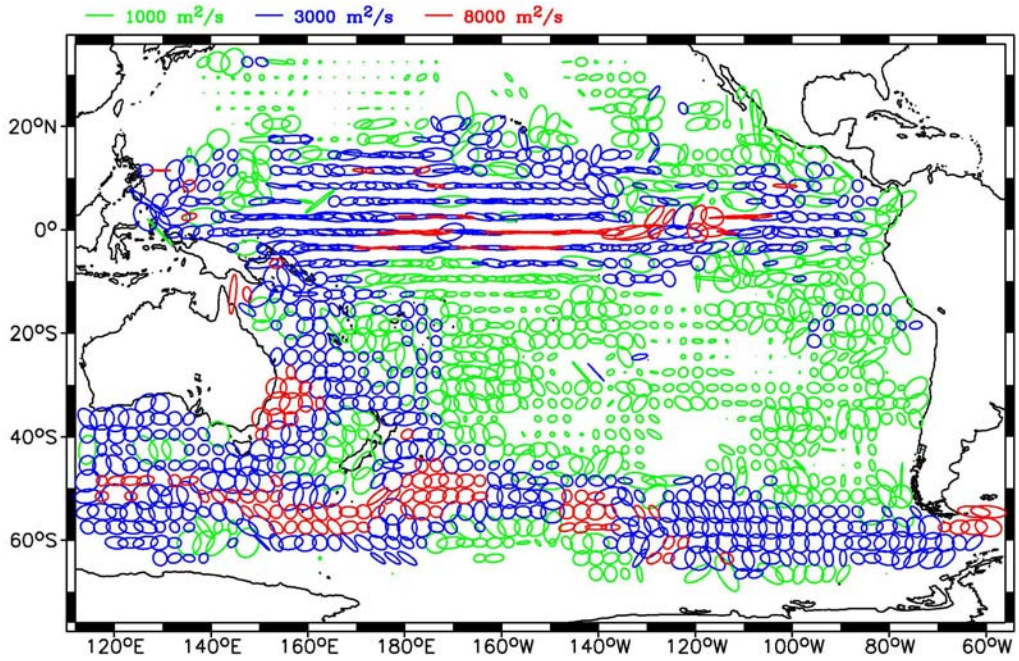

Figure 14. Ellipses of eddy diffusivity K_{ij} at 900 m in the Pacific computed from (7). Ellipse axes (diameters) are proportional to the principal axes of the diffusivity according to the color-coded scales at the top. The diffusivity is large and highly anisotropic in the equatorial zone where zonal dispersion dominates. Otherwise *K* is approximately isotropic. Other regions of high eddy variability are the ACC, EAC and Tasman Current.

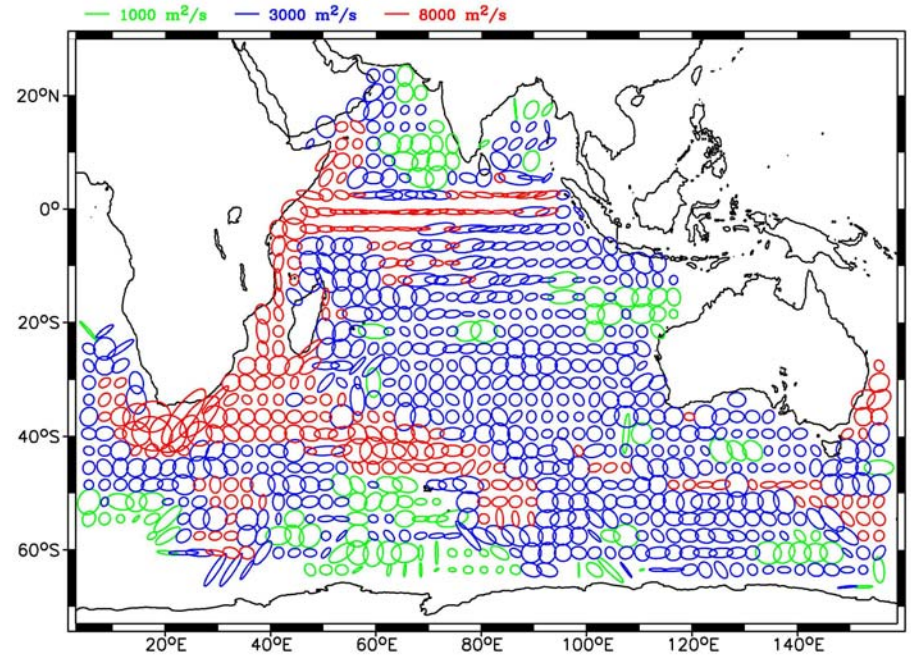

Figure 15. Single-particle eddy diffusivity at 900 m in the Indian Ocean in the same format as Fig. 14. Equatorial variability is anisotropic but less so than in the Pacific. The patterns of eddy diffusivity are analogous to those in the Pacific although generally stronger in the Indian Ocean. Variability is greatest in the "overshoot" region of the Agulhas, not where the velocity is greatest.

6. Objective Mapping: Technique

Both area averages and local function fitting estimate the mean field as a linear filter of the observations of the form $\hat{p} = \mathbf{b}^{\mathrm{T}}\mathbf{d}$ where **d** is the vector of observations, **b** has the filter weights, and $\hat{p}$ is the estimate of one *u* or *v*. A field of such estimates is $\hat{\mathbf{p}} = \mathbf{Bd}$ where many *u* and *v* estimates are combined in **p** and many **b**s are in **B**. The filters used above are based on simple heuristic choices of weights in **B** to relate an estimate to data in a small surrounding region. Objective maps (cf. Bretherton et al., 1975) are of this same linear form but use statistical scale information, rather than heuristics, to select weights **B** that minimize the mean square error $<|\hat{\mathbf{p}}-\mathbf{p}|^2>$. Objective Mapping (OM) strictly minimizes error only if the underlying statistics are accurate but for fields with a reasonable range of energetic scales the weights are not sensitive functions of these statistics and approximate statistics yield only modestly sub-optimal maps.

There are several reasons to move beyond the local filters to OM: the filter weights are matched to the scales of the field so that large-scales can be interpolated into data gaps; kinematic constraints (like horizontal continuity) can be applied to reduce sampling errors; boundary conditions (such as no flow through land masses) can be enforced to further reduce sampling error and produce self-consistent pictures of basin-scale transport; and displacement data can be used to directly estimate velocity and linearly related fields (e.g. a streamfunction). Disadvantages of OM are an indirect connection between details of the analysis and their effect on the results and the difficulty of constructing covariances that reflect spatial inhomogeneity or boundary conditions. These disadvantages can be lessened by noting the connection between OM and fitting to a set of functions.

If **u** is the velocity at each point on a grid, the *N* measured displacements **d** are related to **u** by $\mathbf{d}=\mathbf{Hu}+\mathbf{n}$, where **n** is noise and, as in (1), **H** approximates the time integral relating displacement to velocity $d(m)=\sum_x u[\mathbf{x}(m,t),t]\,\delta t = \sum_x H(m,x)u(x)$. OM estimates any linear functional, **p**, of **u** (e.g. velocity, itself, or streamfunction) as $\hat{\mathbf{p}}=\mathbf{Bd}$ where **B** minimizes $<|\hat{\mathbf{p}}-\mathbf{p}|^2>$ with the estimate

$$\hat{\mathbf{p}}=<\mathbf{p}\mathbf{u}^{\mathrm{T}}>\mathbf{D}^{-1}\mathbf{d}\,, \tag{8}$$

where $\mathbf{D} = <\mathbf{dd}^{\mathrm{T}}> = \mathbf{H} <\mathbf{uu}^{\mathrm{T}}> \mathbf{H}^{\mathrm{T}} + <\mathbf{nn}^{\mathrm{T}}>$ is the data covariance based on the signal covariance $\mathbf{S} = <\mathbf{uu}^{\mathrm{T}}>$ and the error covariance $\mathbf{E} = <\mathbf{nn}^{\mathrm{T}}>$. As discussed above, the un-averaged eddy components displacements are essentially uncorrelated between displacements and approximately isotropic except along the equator where the principal axis is east-west. Thus the noise covariance is approximately diagonal when written in latitude-longitude coordinates.

Here it is assumed that horizontal velocity is related to a scalar field Ψ that is either the streamfunction of a non-divergent horizontal velocity or a geostrophic pressure associated with the continuity relation $\nabla \cdot \mathbf{u} = -\frac{d \ln f}{dy} v$ where f is Coriolis parameter and v is northward velocity. The geostrophic pressure should not be confused with the dynamical pressure – it is simply a streamfunction associated with the geostrophic continuity equation. Unlike dynamical pressure, it must be constant along a land boundary through which there is no flow. The two continuity relations are compared below to gauge sensitivity of results to the assumed continuity relation.

Customarily, the covariances for OM are taken to be spatially homogeneous – a Gaussian or exponential function of position differences is common. Here we are interested in ensuring that the signal field obeys kinematic constraints at coasts. Such a covariance is not homogeneous and cannot be represented by a simple analytic function. Instead, we represent the signal covariance of Ψ between positions $\mathbf{x}_1$ and $\mathbf{x}_2$ as

$$\mathbf{S}(\mathbf{x}_1, \mathbf{x}_2) = \sum_{n}^{M} \sum_{m}^{M} < a(n)a(m) > \psi(\mathbf{x}_1, n)\, \psi(\mathbf{x}_2, m) \qquad \text{or} \qquad \mathbf{S} = \mathbf{F}\,\mathbf{A}\,\mathbf{F}^{\mathrm{T}} \tag{9}$$

where the $\psi(\mathbf{x},n)$ are M basis functions of position $\mathbf{x}$. Conventional homogeneous covariances are of this form (as M approaches infinity) where the columns of $\mathbf{F}$ are sines and cosines and the amplitude covariance $\mathbf{A} = < a(n)a(m) >$ corresponds to the wavenumber spectrum.

Representing the signal covariance as $\mathbf{S} = \mathbf{F}\,\mathbf{A}\,\mathbf{F}^{\mathrm{T}}$ allows objective maps to obey boundary conditions and reflect spatially inhomogeneous statistics by making the functions in $\mathbf{F}$ have these properties. As described in Appendix B, the basis functions are made constant along all land-sea boundaries so that there is no flow through them. Away from these boundaries the functions approximate sinusoids. The wavenumbers of these sinusoids are used to assign the variance of each mode's amplitude $<a^2(n)>$ just as a wavenumber spectrum describes the energy associated with a

wavenumber. Appendix B details how the functions $\psi(\mathbf{x}, n)$ were computed and how the amplitude covariance **A** was adjusted so that the scales of the signal covariance approximate the scales in the function-fit velocities in Figures 12 and 13.

The signal and noise covariances **S** and **E** could be used directly in (8) to compute $\hat{\mathbf{p}}$. The alternate approach used here connects OM to function fitting, connects analysis parameters to properties in the result, and is computationally efficient. As in the local function fitting in Section 4, observations are fit to a linear combination **Fa** of functions using amplitudes **a** that minimize the quadratic cost function of (5), $Q = (\mathbf{d} - \mathbf{HFa})^{\mathrm{T}} \mathbf{E}^{-1} (\mathbf{d} - \mathbf{HFa}) + \mathbf{a}^{\mathrm{T}} \mathbf{A}^{-1} \mathbf{a}$. The manipulation in Appendix C shows that this function fitting leads to a map identical to the objective map from (8) so long as the amplitude and noise covariances **A** and **E** and functions **F** in (5) correspond to the signal and noise covariances in (8). Appendix C discusses this approach to mapping and the way it was applied to insure that $\hat{p}$ is constant along land boundaries.

The approach to estimating mapping error is also novel. While theoretically OM determines mean square error (MSE) directly from the measurement array and the covariances of signal and noise, experimentation shows that the error estimates are strongly dependent on details of the signal covariance, which, in the best of circumstances, is estimated from meager information. Here error is estimated by comparing maps made from subsets of the data. Subsets were constructed by placing the data in chronological order and extracting four groups, each using every fourth sample. In this way each group has roughly the spatial distribution of the full data set but only one quarter of the data. Different combinations of the quarters generate an ensemble of 6 data subsets, each with half the total number of observations. In discussing qualitative features of objective maps, the number of these halves exhibiting a feature is denoted by a fraction in curly brackets. For example, {5/6} indicates that 5 of the 6 subsets showed the feature.

To estimate mapping error, three pairs of maps based on non-overlapping halves of the data were generated using group 1 and 2 vs. 3 and 4, 1 and 3 vs. 2 and 4. etc). The mean square velocity difference between pairs, $<| \hat{\mathbf{u}}_a - \hat{\mathbf{u}}_b |)^2 >$, was averaged over the three pairs. Assuming the sampling errors are uncorrelated, this mean square difference is twice the error of either $\hat{\mathbf{u}}_x$ and 25% of the error of estimates based on all the data. The velocity errors for the objective maps are not identical to those from local function fitting (cf. Figs. 12 and 13), but over any significant area the average errors of the two estimate types are within 30% of each other.

7. Objective Mapping: Results

Figure 16 shows the geostrophic pressure at 900 m for the Pacific and its caption outlines the main elements of the circulation. In addition to clarifying patterns evident in velocity maps, this figure exposes large-scale features that are difficult to detect from velocity alone. Notable are the cyclonic gyre in the Coral and Solomon Seas {6/6} in which the circulation is much greater than the through flow, the ridge (220^{o}-240^{o}E) that disrupts the southern tropical gyre over the East Pacific Rise {5/6}, and a trough along 170^{o}E north of the equator that expands the northern tropical gyre to the north {6/6}. The East Australian Current is strongest at latitudes north of New Zealand {6/6}, but a weaker western boundary current reaches Tasmania and then flows westward south of Australia into the Indian Ocean {6/6}. Remarkably, the eastern boundary of the South Pacific's subtropical gyre occurs 30^{o} west of South America {5/6}. A cyclonic circulation in the Tasman Sea {6/6} and the retroflection of the South Indian Current south of the Tasman Sea comprise the eastern limb of the Indian Ocean's subtropical gyre {6/6} (See Fig. 17).

Figure 17 depicts geostrophic pressure in the Indian Ocean. Eastward flow along the equator separates a trans-basin southern tropical gyre from a northern gyre that encompasses lows the Bay of Bengal {6/6} and the Arabian Sea {4/6}. The subtropical gyre is more than twice as strong as the South Pacific's {6/6}. The SEC flows around both sides of Madagascar to feed a strong Agulhas Current {6/6}. Some of the Agulhas rounds Africa and flows into the South Atlantic {6/6} while most overshoots the African continental slope to 40^{o}S, where it retroflects to form the South Indian Current {6/6}. The eastern limb of the Atlantic's subtropical gyre is evident west of the Agulhas retroflection where it joins the flow around the tip of Africa to form the Atlantic's SEC. The Indian subtropical gyre extends eastward past Australia and, as shown in Fig. 16, has its main eastern boundary upstream of the Campbell Plateau. In view of the mixing expected in the eddy-rich ACC, it is moot whether some of the Atlantic's subtropical gyre reaches this same region.

The flow descriptions in Figures 16 and 17 depend on the float observations, the boundary conditions enforced along landmasses, and the geostrophic continuity relation that links u and v. To gauge the importance of the analysis method, a second set of analyses were made in which horizontal velocity was derived from a streamfunction. The resultant streamfunction maps are shown in Appendix D. The geostrophic and streamfunction velocity maps are essentially identical outside $\pm 10^{o}$ latitude (correlation 0.988) and well correlated (>0.83) in the equatorial zone. In a

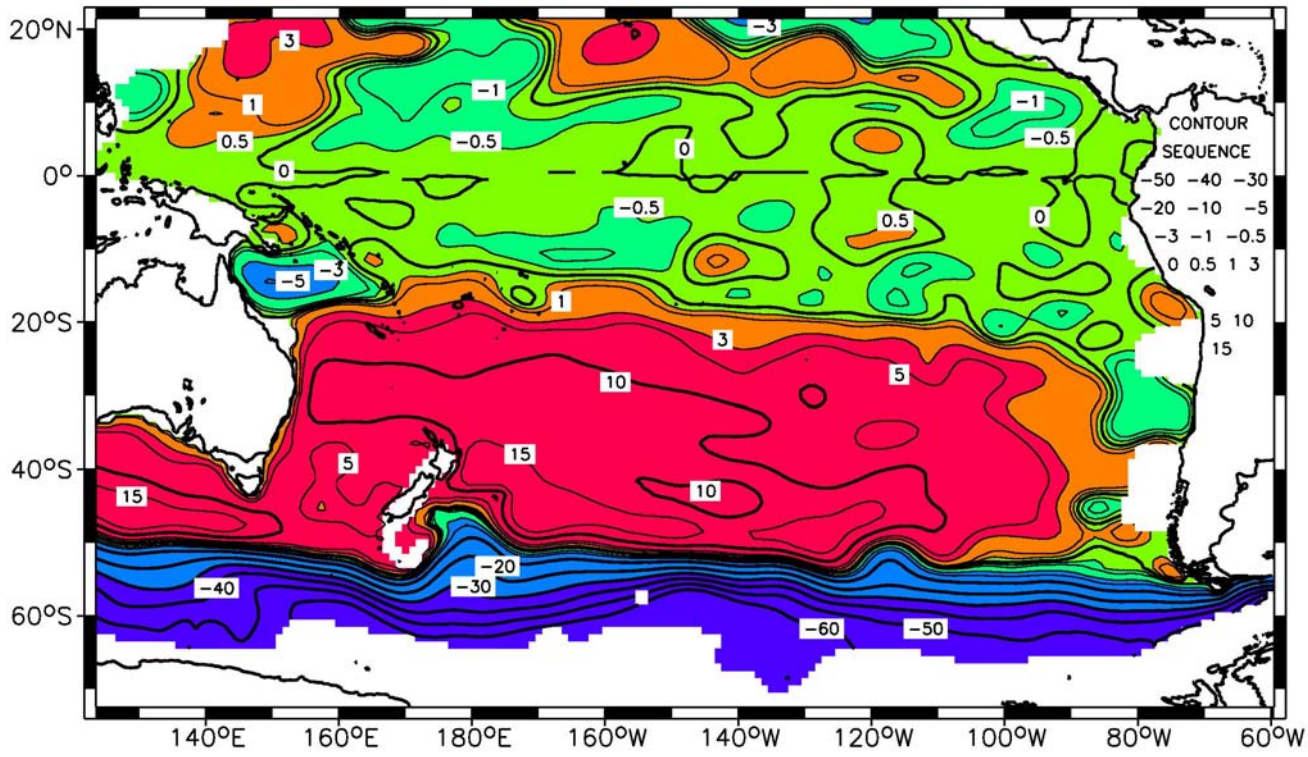

Figure 16. Objectively mapped geostrophic pressure (in centimeters of water, equivalent to dynamic centimeters) for the Pacific Ocean. The irregular contour values are listed over South America. The ridge along 15°N supports a confused intermediate-depth NEC, which apparently feeds the equator without reaching the western boundary. An equatorial ridge separates cyclonic tropical gyres in both hemispheres and supports eastward equator flow {6/6}. The southern tropical gyre is interrupted by a high just west of the East Pacific Rise (EPR) {5/6}. A strong cyclone in the Coral and Solomon Seas {6/6} feeds a weak flow to the equator well east of New Guinea {4/6}. The eastern limb of the subtropical gyre is well west of South America {5/6}. This limb separates from the SPC/ACC between 245° and 260°E over the EPR {5/6}. The East Australian Current (EAC) is strongest at latitudes north of New Zealand but a weaker current flows south past Tasmania and then west into the Indian Ocean, just south of Australia {6/6}. Most of the EAC turns east near 35°N, flowing past New Zealand and then along its east coast to join the ACC at 45°S over Chatham Rise {6/6}. There is a weak cyclonic eddy in the Tasman Sea, some of which feeds the subtropical circulation by flowing south of New Zealand {5/6}. Some eastward flow in the SIC (or ACC) retroflects south of the Tasman Sea and returns to the Indian Ocean (see also Figs. 15 and 17).

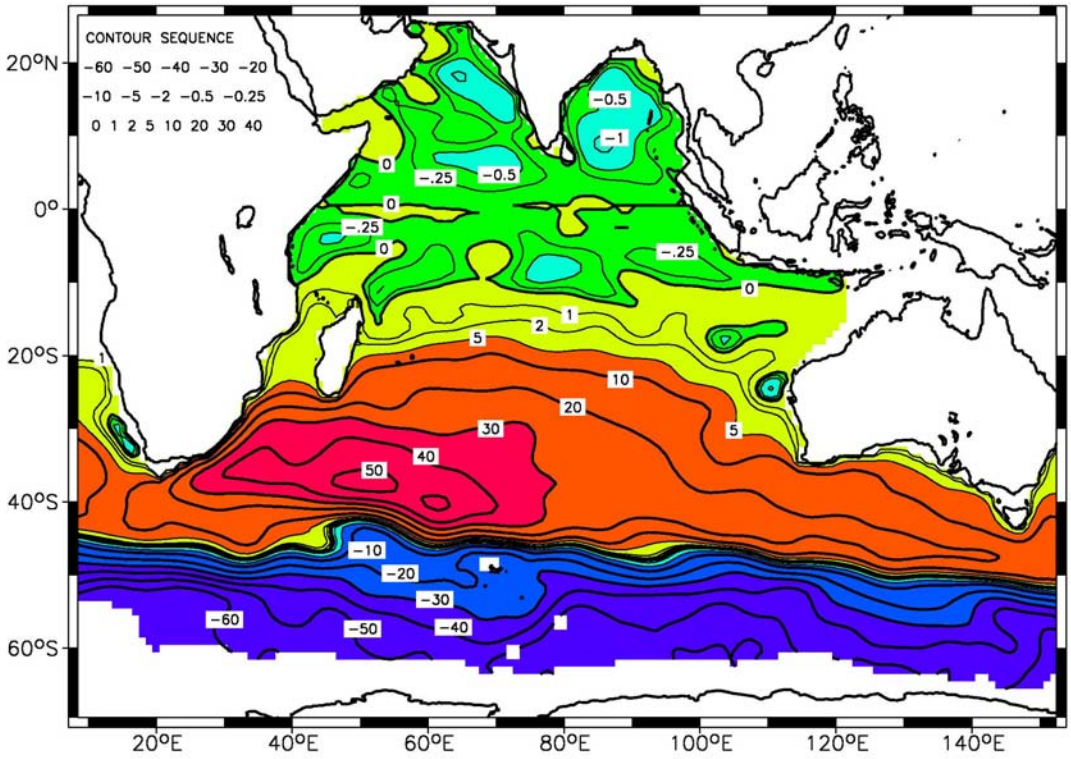

Figure 17. Objectively mapped geostrophic pressure (cm of water) for the Indian Ocean. Lows in the Bay of Bengal {6/6}, the Arabian Sea {5/6}, and the tropical gyre south of the equator support eastward flow along the equator {6/6}. Both tropical gyres include western boundary currents along Africa {6/6}. A weak Indonesian Throughflow {6/6} augments westward flow south of Australia to form an SEC that bifurcates on Madagascar {6/6}. Most of the SEC turns south along Madagascar and crosses the Mozambique Channel to form the intermediate-depth Agulhas. The rest of the SEC flows north around Madagascar and forms a western boundary current in the Mozambique Channel that adds to theAgulhas {6/6}. The Agulhas accelerates sharply, overshoots Africa and retroflects to form the SIC but some escapes into South Atlantic in a stream that separate immediately from the African Coast {6/6}. (The band of pressures between 0 and 5 cm marked yellow that continues along the African east coast is lost in the graphic). The ACC/SIC splits behind Del Cano Rise (45^{o}E) and refocuses behind the Kerguelen Plateau (70^{o}E), flows south of Australia before some retroflects south of the Tasman Sea {6/6} as shown in Fig. 16. Some the South Atlantic Current flows east past the tip of Africa, retroflects south of the Tasman Sea, and re-enters the Atlantic from the Agulhas, making Campbell Plateau (50^{o}S, 170^{o}E) the eastern boundary for part of the South Atlantic's subtropical gyre.

similar vein, maps were prepared with different basis functions for the objective analysis. Even such a dramatic change as making the landmass pressure functions (see Appendix C) decay exponentially over 5^o of latitude/longitude from the coast where they have unit value had no significant effect. Similarly, increasing the length scale in the amplitude spectrum of basis functions had negligible effect beyond a predictable impact on smoothness.

8. Pathways and Transport

The pathways of large-scale transport disclosed by floats resemble the patterns of near-surface flow. Outside the near equatorial zone ($\pm 10^o$) circulation is dominated by subtropical gyres bounded by strong eastward flow in the Antarctic Circumpolar Current (ACC) and the South Indian Current (SIC) or South Pacific Current (SPC). The Indian Ocean's subtropical gyre is at least twice as strong as the South Pacific's, making the powerful intermediate-depth Agulhas Current much stronger than the East Australia Current. It is remarkable that the eastern limbs of the southern subtropical gyres in all three basins occur away from land and one wonders how this relates to the concept that Sverdrup Transport can be integrated west from eastern boundaries.

In both basins there is a ridge of pressure along the equator and cyclonic tropical gyres to both sides, reflecting a general eastward equatorial flow. The tropical gyres are seriously distorted by bathymetry. A ridge of high pressure roughly overlying the East Pacific Rise breaks up the South Pacific tropical gyre while the North Pacific tropical gyre has a bulge to the north over a large region of sea mounts centered near 18^oN, 175^oE. The Indian subcontinent splits the North Indian tropical gyre, forming separate cyclones in the Bay of Bengal and Arabian Sea. The Bengal Bay cyclone is poorly sampled and the Arabian Sea cyclone, although adequately sampled, is complex and does not appear to have a strong western boundary current. The South Indian tropical gyre is split by a ridge of higher pressure overlying the shallow bathymetry running northeast from Madagascar, along the eastern flank of the Somali Basin.

The ACC and its subtropical companions the SIC and SPC trend southward across both the Pacific and Indian basins with significant jumps northwards behind the Del Cano Rise (47^oS, 45^oE), Kerguelen Plateau (52^oS, 70^oE), Campbell Plateau (52^oS, 170^oE) and, of course, the tip of South America (not shown; see Gille [2003]). Data coverage is inadequate to describe much south of the ACC except southward flow into the Ross Sea near 65^oS, 140^oW (see Figs. 10 & 12).

Can objective mapping constrained by a continuity relation and no-flow-through-land boundary conditions combine data throughout the basin to make accurate mean transport estimates? It is, of course, impossible to directly measure mean transport without observations at many depths. Combining float-measured velocity at one level with hydrography holds the promise of deducing such transport, but for now discussion must be limited to transport per unit depth near 900 m. Zonal differences of pressure and/or streamfunction imply net meridional flows through the Indian and Pacific Oceans. Similar integrated velocities, measured in transport per unit depth, can potentially be computed for the Indonesian Throughflow, the Tasman Sea and the Mozambique Channel. Insufficient observations in the southern half of the circumpolar Southern Ocean preclude transport estimates across that ocean.

Horizontal continuity and no-flow-through-landmasses boundary conditions potentially brings all the data in a basin to bear on measuring net flow between landmasses but the analysis, itself, is in question. The boundary conditions may be wrong because vertical motion along a sloping boundary allows horizontal flow to cross isobaths and large-scale analyses frequently have dynamic-height contours that intersect coasts (cf. Reid, 1997 and 2003). The geostrophic continuity equation $\partial_x u + \partial_y v = -\beta v / f$ is likely to distort transport estimates when applied near the equator while horizontal nondivergence may fail everywhere. Finally, the objective mapping method requires that the RMS net inter-landmass flows be estimated. Analyses employing different continuity equations, different subsets of the data, and different analysis parameters were used to estimate transport per unit depth at 900 m and to test the ability of the analysis to enlist data throughout a basin to estimate the transport through it.

Analyses were based on geostrophy or horizontal nondivergence with, in both cases, no flow across land boundaries. Experimentation with the wavenumber spectrum describing the energy of interior modes (see Appendix B for definitions of different mode types) showed no significant effect beyond the expected link of smoothness and spectral cutoff scale. The a priori estimates of strength of the landmass modes, however, had an impact on some transports. The standard analysis (pictured in Figs. 16 and 17) was based on the a priori RMS amplitudes listed in Appendix B, which corresponded to the author's guess at plausible sizes for inter-landmass transports. Table 1 lists (a) transport per unit depth at 900 m between various landmasses, (b) sampling errors estimated, as above, using subsets of the data, and (c) sensitivity to $\pm 50\%$ changes in the a priori RMS

amplitudes of all landmass modes. The units of transport per unit depth are 1000 m^2/s. For example, a change of Q_{GEO} or $\Delta\psi$ of one unit corresponds to a change in the transport above 900 m of 0.9 Sverdrups.

In Table 1, the transports per unit depth through the Tasman Sea between Australia and New Zealand, through the Mozambique Channel, out of the Indonesian Throughflow into the Indian Ocean, and through the South Indian Ocean, all appear to be reasonably well measured with acceptably small sampling error and sensitivity to a priori assumptions. The geostrophic Q_{GEO} and streamfunction, $\Delta\psi$, are generally consistent although, because Q_{GEO} between the same landmasses varies as $1/f$, there must be discrepancies over a range of latitudes. The table includes consensus estimates of transport and an uncertainty that summarizes the variability between different data subsets and the discrepancy between geostrophic and nondivergent calculations. The Mozambique Channel uncertainty of 1000 m^2s^{-1} corresponds to a velocity uncertainty of 1-2 mm s^{-1} over a typical channel width while the uncertainty of 500 m^2s^{-1} across the South Indian Ocean corresponds to less than 0.1 mm s^{-1} across the width of the ocean. It is encouraging that the Indonesian Throughflow and South Indian transports are comparable.

Table 1 also lists the results for transport per depth through the South Pacific (Australia to the Americas), through the North Pacific (Asia to the Americas) and into the Indonesian Throughflow from the Pacific. No consensus from these results was found. Except for the geostrophic calculation in the South Pacific, the sensitivity to a priori parameter choices is large and there is significant discrepancy between geostrophic and nondivergent continuity constraints. The North Pacific and Throughflow results depend on establishing pressure or streamfunction along the Asian coast and the measurement coverage in Figure 1 shows low data density in the western tropical Pacific. The problem with the calculations for the South Pacific is the discrepancy between Q_{GEO} and $\Delta\psi$ and the sensitivity of the latter to a priori parameters. It is tempting to dismiss the nondivergent calculation on the grounds that its difference from the more accurate geostrophic continuity constraint becomes large over the large range of latitudes involved in the South Pacific, making the entire data-fitting process unreliable. At least the discrepancy proves the obvious: no-flow-through-land boundary conditions can only improve the analysis if an accurate continuity relation is used.

Net Flow Between Landmasses

Region (Direction)	$\Delta P \pm$ Samp	Prior	Q_{GEO}	Lat	$\Delta\psi \pm$ Samp	Prior	Q
Tasman Sea - 40°S (to N)	-6.12 ± 0.8	0.7	-6.4	40°S	-7.8 ± 1.4	1.2	-7 ± 1
Mozambique Channel (to S)	2.14 ± 0.5	0.8	4.2	20°S	4.2 ± 1.1	2.1	4 ± 1
Indian Throughflow (to IO)	0.35 ± 0.15	0.17	1.3	10°S	1.1 ± 0.4	0.2	1.2 ± 0.3
South Indian Ocean (to S)	0.35 ± 0.15	0.17	0.5	30°S	1.1 ± 0.4	0.2	0.7 ± 0.5
South Pacific Ocean (to N)	0.17 ± 0.13	0.00	0.2	30°S	1.7 ± 0.5	1.4	—
North Pacific (to N)	0.03 ± 0.00	0.03	0.1	15°N	-0.3 ± 0.1	0.3	—
Pacific Throughflow (to IO)	-0.20 ± 0.13	0.03	-1.5	15°N	1.9 ± 0.6	1.7	—

Table 1. Inter-landmass transport per unit depth. First column describes the water body bounded by landmasses and the direction to which positive transport flows. The next 4 columns refer to geostrophic calculations. "$\Delta P \pm$ Samp" is the geostrophic pressure difference in cm of water (≈ 100 Pa) and its sampling error deduced from data subsets; a positive value corresponds to geostrophic flow in the direction in column 1. "Prior" is the RMS change in ΔP when the a priori RMS amplitudes of landmass modes are changed by $\pm 50\%$. "Q_{GEO}" is the implied geostrophic transport per unit depth in 1000 m^2/s at the latitude "Lat." The next 2 columns refer to calculations with nondivergent horizontal flow. "$\Delta\psi \pm$ Samp" is the streamfunction difference, or transport per unit depth (in 1000 m^2/s), and its sampling error. A positive $\Delta\psi$ corresponds to flow in the direction in column 1. "Prior" is the sensitivity to $\pm 50\%$ changes in a priori RMS landmass-mode amplitudes. The last column is the consensus transport per depth and its likely error; a dash indicates absence of a consensus.

9. Conclusion

The basin-scale scope of the WOCE float program expands considerably on earlier direct measurement programs that were regional. This expansion was made economically feasible by

autonomous floats that use satellite navigation and data relay and by using floats to measure mean velocities over several days rather than trying to track the details of quasi-Lagrangian trajectories.

Previous analyses of basin-scale circulation have been based on hydrographic surveys with only occasional comparison with direct measurement. Appendix E compares the geostrophic pressure maps in Figures 16 and 17 with dynamic height maps for the Pacific by Reid (1997) and the Indian Ocean by Reid (2003). The general patterns and strengths of flow in both basins agree remarkably between floats and hydrography combined with Reid's estimate of a reference velocity. Agreement is best where flows are strong, like the ACC and southern hemisphere subtropical gyres, and less striking in the tropical gyres. In the tropics the general features of a high-pressure ridge along the equator separating tropical cyclones is found in both analyses in both gyres, but Reid's gyres are both smoother and stronger (and his sampling density is lower). The largest differences are found in the western parts of the southern Indian tropical gyre and the northern tropical gyre in the Pacific.

Where floats and hydrography agree, it is likely that the circulation is correct since the methods are independent. In the tropics the signal-to-noise ratio is lower for both methods: the circulation signal is masked by internal wave noise in hydrography while the increasing time scale of temporal variability confuses averaging float velocities. The floats of the Argo program (Roemmich and Owens, 2000) are now adding to the sampling in this region and in a few years it should be possible to better separate the general circulation from variability.

Methodology can also improve the accuracy of circulation mapping. Two avenues present themselves: (a) use additional physical parameters (e.g. geostrophic shear, velocity at other levels, and/or water-property tracers) to further constrain the analysis; (b) improve the representativeness of the basis functions used to construct the signal covariance **S** of (9). Additional parameters and observations could be incorporated by expanding the quadratic cost function (5) within the objective analyses framework or by assimilating hydrographic and float data into a ocean general circulation model (cf. Stammer et al., 2003).

Within the function-fitting context, the number of functions whose mean-flow amplitudes can be accurately determined depends on the number of observations and temporal variability. The more efficient functions are (in terms of variance described per function), the more accurate will be the result. Here we have used simple non-dynamical velocity functions to enforce either

geostrophic or nondivergent continuity on the horizontal velocity while obeying no-flow-through-land boundary conditions. Mean flow maps based on geostrophy (Figures 16 and 17) and on a streamfunction (Appendix D) are more different than are analyses that use moderately different numbers of functions or different spectral shapes. Improvements to analysis accuracy then depend on employing functions that efficiently describe the signal in few functions and this requires that they accurately capture the kinematics of that signal.

It is promising to use numerical general circulation models to generate signal covariances that optimize objective analysis. By employing ranges of plausible surface forcing fields, parameterizations for unresolved processes, and specific numerical details, one could generate an ensemble of mean circulations, each with a rough estimate of its probability. From this a full signal covariance would follow directly. (Indeed, this procedure is the logical basis for applying objective analysis to estimating a signal that is a mean field – the signal covariance does not describe that single mean field but rather of the ensemble of possible mean fields taking into account their a priori probability.) In this proposed methodology the most realistic analysis would be selected by the data as a linear combination of model solutions.

Acknowledgment. This work was carried out while the Instrument Development Group at SIO perfected the ALACE and SOLO floats. Their hard work and skillful technical solutions were essential to success. Some ALACE floats were constructed by Webb Research Corp., but most were assembled at SIO from parts provided by Webb. I owe particular thanks to the many scientists who deployed these floats from research cruises and made the project feasible. The WOCE float data provided by Prof. Steve Riser (University of Washington) were very valuable as were the EOFs of seasonal variability provided by Dr. Benyang Tang (Jet Propulsion Laboratory). The ALACE float was developed under Office of Naval Research support, WOCE deployments were supported by the National Science Foundation, development of the SOLO float and deployments in the tropical Pacific were supported by NOAA's Office of Global Programs, and this analysis was completed as part of the ECCO project of the National Ocean Partnership Program.

Appendix A. The data

A brief summary of the way autonomous floats sample will help explain the imperfections in the data. Davis et al. (1991) describe the ALACE float, from which most data used here were obtained. SOLO floats, described by Davis et al. (2001), provided some later data in the tropical Pacific; their external functionality is the same as the ALACE. Prof. Steve Riser (University of Washington) provided 104 float-years of data from the 53 North-Pacific RAFOS floats described in Riser (2004). Fourteen float-years of this data from 1000 m depth were used to augment the autonomous floats in the tropical North Pacific. These trajectories were broken into sequential 10-day displacements and then treated like autonomous float data.

Most autonomous floats were programmed to stay submerged for 25 days and to then surface for a period of about 21 hours while signals were broadcast to System Argos satellites. This relatively long surface period was chosen to provide enough surface positions that surface drift could be objectively extrapolated to the times at which the float surfaced and submerged. Typically, there were a few hours after surfacing and before submerging when no Argos satellites were overhead. Davis et al. (1991) describe the extrapolation procedure. The accuracy of extrapolated positions depends strongly on the surface currents. An error of 2 km is typical, which contributes an error of O(2 mm s^{-1}) when the submerged time is 25 days. When mapping the mean circulation, the velocity of mesoscale eddies represents a noise superposed on the signal of interest. The approximately random surface drift error is much smaller than this noise and is, therefore, negligible.

The velocities used here are based on the extrapolated submergence and surfacing positions being the beginning and end of the at-depth displacement. In a sheared current, lateral motion as the float descends and ascends is another a source of velocity error. The float descends at about 15 cm s^{-1} near the surface and arrives within 100 m of its target depth in about 2.5 hours; the ascent is at ~ 25 cm s^{-1} and takes little more than 1 hour. A linear shear of 30 cm s^{-1} between the surface and observation depth would contribute an error of O(1 mm s^{-1}). The impact is smaller if the shear is concentrated near the surface so we estimate the error is typically less than 0.2% of the surface current relative to the observation depth. Unlike the effect of imperfectly measured surface drift or eddy shear, the mean shear error is potentially a bias not reduced by averaging. To a considerable

extent this could be corrected using mean geostrophic shear estimated from climatological densities. This has not been done because the bias is insignificant compared with measured currents.

Because they do not follow vertical water motion, submerged floats can ground and even more become grounded when surface flow carries them into shallow water. Data is searched for likely grounding by comparing depth along float trajectories with ETOPO5 bathymetry and by examining the time series of velocity for slowing that occurs simultaneously with a float entering shallow water. Float displacements that occur while a float is believed to be grounded are excluded from statistical analyses.

Most WOCE floats were targeted for 1000 m depth but drifted slowly upwards over their typical life of 5 years. We suspect this low vertical drift is a consequence of corrosion of the unpainted anodized aluminum buoy hull. Table A1 shows the distribution of observation depths for all floats. For less than 1% of the subsurface displacements the pressure readings appeared to be seriously in error. In such cases, the displacement was assigned a depth inferred from a combination of interpolating from neighboring readings and comparing measured temperature with climatology.

Prior to the analyses presented here, the velocities from each at-depth displacement were corrected from the measured depth to 900 m depth using geostrophic shear from the World Ocean Data climatology (Ocean Data Laboratory, 1998). To prevent near-equatorial geostrophy from magnifying the effect of small density errors, the geostrophic shear was additionally smoothed when a shear correction was unusually large compared with nearby shears. Velocities were, as described in Section 2, transferred to a one-degree grid such that shear corrections were never computed closer than 0.5^{o} to the equator.

Ocean	Number	550	650	750	850	950	1050	1150	1200 +
Pacific	23,876	10	7	15	26	18	16	1	7
Indian	19,899	5	10	22	37	21	5	0	0

Table A1. The number and depth distribution of the float observations. Table shows percentage of observations in the 100 meters centered on the depth listed.

Appendix B. The functions F for objective mapping

As discussed in Section 6, the objective mapping procedure used here is based on a signal covariance for the geostrophic pressure or streamfunction $\mathbf{S}=\mathbf{F}\mathbf{A}\mathbf{F}^{\mathrm{T}}$, which is constructed from a set of *M* scalar functions $\psi(\mathbf{x},n)$ that are components of Ψ in the columns of **F.** These functions are derived from, either the geostrophic pressure or streamfunction. "Interior" functions are solutions of Poisson's equation

$$\nabla^2\psi(\mathbf{r},n)=\exp(i\mathbf{k}_n\cdot\mathbf{r}) \qquad \text{with} \qquad \psi=0 \quad \text{on all boundaries}$$

where the functions depend on the wavenumbers $\mathbf{k}_n$. "Landmass" modes are solutions of Laplace's equation and take unit value on one coast and zero on all other boundaries; these are used to allow transport between different landmasses. "Open boundary" functions are used to describe flow through one boundary. These modes are also solutions of Laplace's equation with homogeneous boundary conditions on all boundaries save the open boundary of interest where they are one component of a sine series representing Ψ.

The functions ψ were computed on a 1^{o} grid with boundaries representing the intersection of a smoothed topography with the 700 m depth horizon. The Pacific and Indian oceans were treated separately but shared a common area south of Australia. The grids, prescribed landmasses, and functions used to span open boundaries are described in Table B1. The largest wavelengths used to force Poisson's equation equaled the grid dimensions. The sine series describing open boundaries have a longest half-wavelength equal to open-boundary width. For geostrophic calculations, the interior and open-boundary "pressure" functions ψ_n were multiplied by latitude before velocity functions were computed using geostrophy.

The amplitude covariance **A** was taken to be diagonal reflecting ignorance of any relation between different functions. The diagonal elements of **A** are the a priori estimates of the mean-square size of each amplitude. **A** is the equivalent of the wavenumber spectrum for a statistically homogeneous fields. The amplitude variance A_{nn} of interior-forced modes was made to vary with the forcing wavenumber **k** as $\exp[-(\mathbf{k}_n\cdot\mathbf{L})^2/2]$. Far from boundaries, the modes approximate scaled forcing functions, describing a spatially lagged covariance that varies as $\exp[-(\Delta x/L_x)^2/2-(\Delta y/L_y)^2/2]$ where Δx and Δy are spatial separations measured in degrees

of longitude and latitude, respectively. With the spectral shape determined, the RMS amplitudes are set by RMS velocity U_{RMS}. Experiments with different L_x, L_y and U_{RMS} were explored but all results presented here were performed with the choices listed in Table B1. The amplitude variances in **A** associated with open boundaries were specified from a velocity spectrum that decreased as $|\mathbf{k}|^{-2}$ and had the total RMS velocity listed in Table B1.

South and Tropical Pacific L_x=5°, L_y=3.5°, U_{RMS}=5 cm s^{-1}					
Grid 114.5°E – 59.5°W, 72.5°S – 32.5°N	N_{FNX} = 2041	N_{KX} = 25	N_{KY} = 20		
Land Mass	Antarctica	Australia / N. Guinea	Asia	Americas	Antarctica
N_{OBC} (U_{OBC})	8 (10 cm s^{-1})	2 (3 cm s^{-1})	21 (2 cm s^{-1})	3 (15 cm s^{-1})	
Indian Ocean L_x=4°, L_y=3°, U_{RMS}=5 cm s^{-1}.					
Grid 5.5°E – 155.5°E, 69.5°S – 26.5°N	N_{FNX} = 2033	N_{KX} = 20	N_{KY} = 20		
Land Mass	Antarctica	Africa / Asia	Australia	Antarctica	
N_{OBC} (M_{OBC})	12 (10 cm s^{-1})	1 (-)	14 (10 cm s^{-1})		

Table B1. The grids for objective mapping. N_{FNX} is the total number of functions fit. N_{KX} and N_{KY} are the numbers of distinct wavenumbers in the east-west and north-south directions, respectively. N_{OBC} is the number of functions used to span the open boundary between the landmasses above. U_{OBC}, is the RMS velocity distributed across the N_{OBC} open-boundary modes. In the Indian Ocean the Asia-Australia gap is only 1° and is spanned by a single velocity value.

The RMS amplitudes associated with landmass modes were based on assumed RMS transports per unit depth between different landmasses. Experimentation showed that these a priori estimates affected some inter-landmass transports as described in Section 8. Such experiments were perturbations of the standard analysis (e.g. Figs. 16 and 17) based on the RMS land-mode amplitudes listed in Table B2. In each basin one land mass was held at zero pressure or streamfunction.

Pacific Ocean	Australia	N. Zealand	Asia	Antarctica	Americas
RMS Pressure Amp (cm H_2O)	1.2	5.4	0.1	31.6	0
RMS Streamfunction Amp (1000 m^2s^{-1})	1.7	5.7	1.1	27.8	0
Indian Ocean	Australia	Madagascar	Kerguelen	Antarctica	Africa/Asia
RMS Pressure Amp (cm H_2O)	0.9	0.9	15.9	37.9	0
RMS Streamfunction Amp (1000 m^2s^{-1})	3.3	2.2	16.5	33.3	0

Table B2. RMS amplitudes of landmass modes in the standard objective analysis.

Appendix C. Objective mapping and function fitting

Objective mapping uses a vector of observations **d** to form the linear estimate $\hat{\mathbf{p}} = \mathbf{d}^{\mathrm{T}} \mathbf{D}^{-1} < \mathbf{dp} >$ that minimizes the expected square error $E = <|\hat{\mathbf{p}} - \mathbf{p}|^2>$. The data-data mean product $\mathbf{D} = < \mathbf{dd}^{\mathrm{T}} > = \mathbf{HSH}^{\mathrm{T}} + \mathbf{E}$ is the sum of sampled-signal and noise mean products. When **d** and **p** are zero mean and joint normally distributed, then $\hat{\mathbf{p}}$ is a maximum likelihood estimate (cf. Bretherton et al., 1975). When the signal mean product is $\mathbf{S} = \mathbf{FAF}^{\mathrm{T}}$ and the variable to be estimated is the signal field, itself, the objective-mapping estimate can be written

$$\hat{\mathbf{s}} = \mathbf{FAG}^{\mathrm{T}} (\mathbf{G A G}^{\mathrm{T}} + \mathbf{E})^{-1} \mathbf{d} \ . \qquad \text{(C1)}$$

where **G** = **HF** has as columns the differences of the fitting functions that approximates the integral of velocity along an inferred path for a displacement as in (1).

The function-fitting procedure finds the estimate $\tilde{\mathbf{p}} = \mathbf{F}\tilde{\mathbf{a}}$ that minimizes the generalized measure of misfit *Q* of (5), which measures the misfit relative to the expected observational noise **n** plus the size of the amplitude $\tilde{\mathbf{a}}$ relative an a priori estimate of its size. If $\tilde{\mathbf{a}}$ and **n** are independent and normally distributed, *Q* is the negative of the log joint probability of $\tilde{\mathbf{a}}$ and the error **n**, so that $\tilde{\mathbf{p}}$ is a maximum likelihood estimate. *Q* is minimized by

$$\tilde{\mathbf{p}} = \mathbf{F} (\mathbf{A}^{-1} + \mathbf{G}^{\mathrm{T}} \mathbf{E}^{-1} \mathbf{GF})^{-1} \mathbf{G}^{\mathrm{T}} \mathbf{E}^{-1} \mathbf{d} \qquad \text{(C2)}$$

Since the objective mapping (C1) and the function fit (C2) are both maximum likelihood estimates, it is not surprising that they are, in fact, different algorithms for calculating the same estimate. This is shown by the following manipulation:

$$\hat{\mathbf{p}} - \tilde{\mathbf{p}} = \mathbf{F}\,[\,\mathbf{A}\mathbf{G}^T(\mathbf{G}\mathbf{A}\mathbf{G}^T + \mathbf{N})^{-1} - (\mathbf{A}^{-1} + \mathbf{G}^T\mathbf{E}^{-1}\mathbf{G})^{-1}\,\mathbf{G}^T\mathbf{E}^{-1}]\,\mathbf{d}$$

$$= \mathbf{F}\,(\mathbf{A}^{-1} + \mathbf{G}^T\mathbf{E}^{-1}\mathbf{G})^{-1}\,[(\mathbf{A}^{-1} + \mathbf{G}^T\mathbf{E}^{-1}\mathbf{G})\,\mathbf{A}\mathbf{G}^T(\mathbf{G}\mathbf{A}\mathbf{G}^T + \mathbf{E})^{-1} - \mathbf{G}^T\mathbf{E}^{-1}\,]\,\mathbf{d}$$

$$= \mathbf{F}\,(\mathbf{A}^{-1} + \mathbf{G}^T\mathbf{E}^{-1}\mathbf{G})^{-1}\,[(\mathbf{A}^{-1} + \mathbf{G}^T\mathbf{E}^{-1}\mathbf{G})\,\mathbf{A}\mathbf{G}^T - \mathbf{G}^T\mathbf{E}^{-1}(\mathbf{G}\mathbf{A}\mathbf{G}^T + \mathbf{E})](\mathbf{G}\mathbf{A}\mathbf{G}^T + \mathbf{E})^{-1}\mathbf{d}$$

$$= \mathbf{F}\,(\mathbf{A}^{-1} + \mathbf{G}^T\mathbf{E}^{-1}\mathbf{G})^{-1}\,[\mathbf{G}^T + \mathbf{G}^T\mathbf{E}^{-1}\mathbf{G}\mathbf{A}\mathbf{G}^T - \mathbf{G}^T\mathbf{E}^{-1}\,\mathbf{G}\mathbf{A}\mathbf{G}^T - \mathbf{G}^T\,]\,(\mathbf{G}\mathbf{A}\mathbf{G}^T + \mathbf{E})^{-1}\,\mathbf{d}$$

$$= 0 \qquad \text{(C3)}$$

While the two algorithms are equivalent, there are advantages to working with the function-fitting form (C2) when, as it is in the present case, the observational noise is uncorrelated so that **E** is diagonal and trivially inverted. The computational effort is then in inverting **A** and $\mathbf{A}^{-1} + \mathbf{F}^T\mathbf{H}^T\,\mathbf{E}^{-1}\mathbf{H}\mathbf{F}$, both of order the number of amplitudes in **a**. When noise is significant, several independent data within each resolution scale are needed to accurately map a point. Thus the dimension of **a** should be much smaller than the dimension of **d** and inverting the data-data mean product **D** in the objective mapping form (C1) is more difficult than evaluating (C2). While the classical objective estimate (C1) can be used with a signal covariance based on functions as $\mathbf{S} = \mathbf{F}^T\mathbf{A}\mathbf{F}$, once the functions have been found it is natural to employ the alternative (C2).

The estimate (C2) is closely related to the familiar estimate made by fitting a set of functions to the data using a least-square-misfit criterion, which gives the estimate

$$\breve{\mathbf{a}} = (\mathbf{G}^T\mathbf{G})^{-1}\,\mathbf{G}^T\mathbf{d} \qquad \text{(C4)}$$

The analogous amplitude estimate from (B2) is

$$\tilde{\mathbf{a}} = (\mathbf{A}^{-1} + \mathbf{G}^T\,\mathbf{E}^{-1}\mathbf{G})^{-1}\,\mathbf{G}^T\mathbf{E}^{-1}\mathbf{d}\,. \qquad \text{(C5)}$$

The features added in the objective formulation are most easily seen when **E** is diagonal with equal diagonal elements ε. Then (B5) becomes

$$\tilde{\mathbf{a}} = (\,\varepsilon\,\mathbf{A}^{-1} + \mathbf{G}^T\mathbf{G})^{-1}\,\mathbf{G}^T\mathbf{d}\,, \qquad \text{(C6)}$$

This is a "tapered" form of (B4) in which the estimated amplitudes are reduced by addition of $\varepsilon\,\mathbf{A}^{-1}$ to the matrix to be inverted. This added term is a noise-to-signal energy ratio. The effect of adding

the amplitude size factor to the cost function Q of (5) is to convert a least-square-misfit estimate into an estimate $\tilde{\mathbf{p}}$ in which each amplitude "fades" toward zero when the noise-to-signal is high, rather than chasing the noise.

D. Streamfunction Mapping

In order to determine the sensitivity of mapped circulation to the continuity relation employed, objective maps were computed using horizontal non-divergence, no-flow-through-land boundary conditions and the same signal-covariance parameters listed in Appendix B. The results are presented in Figures D1 and D2 in terms of the streamfunction Ψ defined by $u=-\partial\Psi/\partial y$ and $v=\partial\Psi/\partial x$ for the Pacific and Indian Oceans, respectively.

The patterns of circulation are very similar to those obtained by mapping with a geostrophic horizontal velocity continuity relation: outside the equatorial zone $|y|<10^{O}$ the vector correlation is 0.988 in both the Indian and Pacific Oceans while near the equator the correlation is 0.83 in the Pacific and 0.85 n the Indian Ocean. Nevertheless, as Table 1 shows, there are substantial differences between the largest scales between geostrophic and nondivergent calculations.

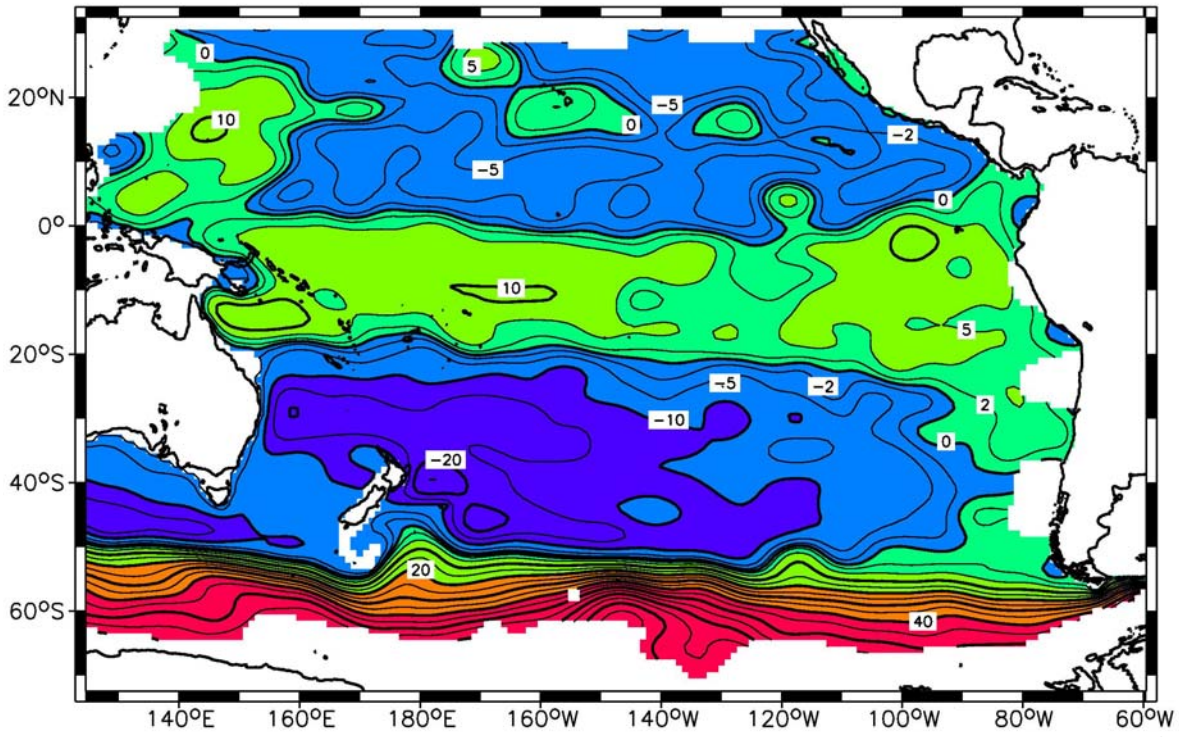

Figure D1. Streamfunction for Pacific Ocean mean circulation at 900 m. Units are 1000 m^2s^{-1} and streamfunction differences correspond to transport per unit depth. Contour interval is 5000 m^2s^{-1} with additional contours at ± 2000 m^2s^{-1}.

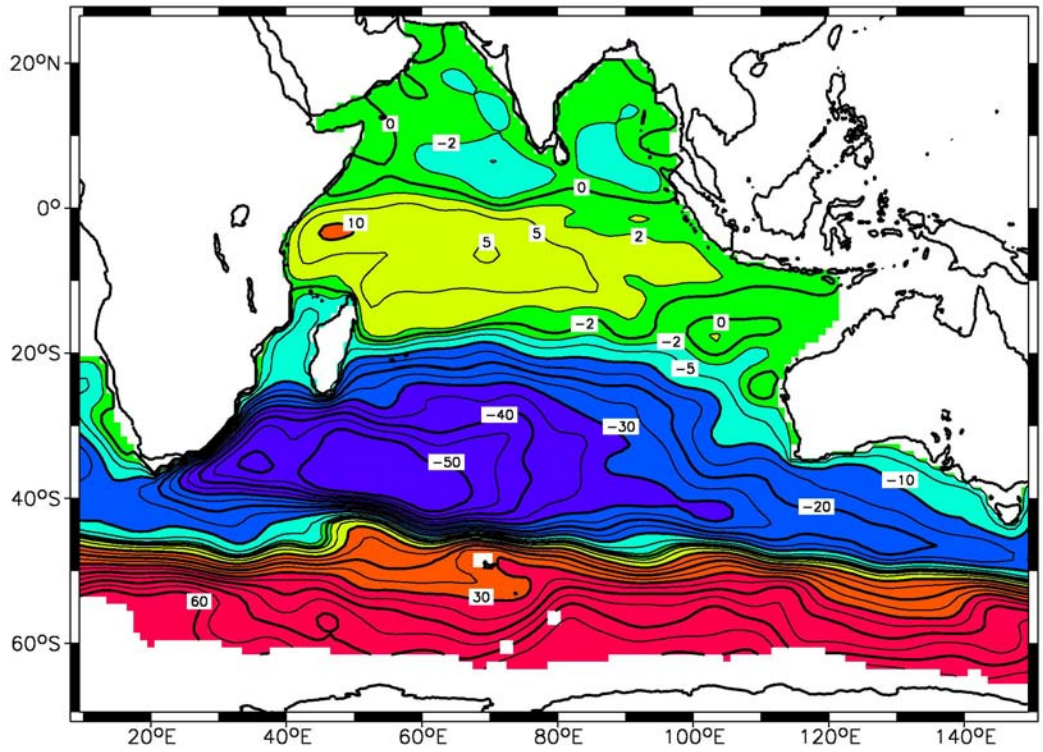

Figure D2. Streamfunction for Indian Ocean mean circulation at 900 m. Contours are labeled in units of 1000 m^2s^{-1} with an interval of 5000 m^2s^{-1} plus contours at $\pm$ 2000 m^2s^{-1}.

E. Comparison with Hydrographic Analyses

The geostrophic pressure maps in Figures 16 and 17 can be compared with absolute dynamic height maps for the Pacific by Reid (1997) and the Indian Ocean by Reid (2003). Reid's figures for 800 m depth are reproduced in Figures E1 and E2. These show the main circulation elements to agree in position and strength, although Reid's tropical circulation is generally stronger by a factor of two.

In the Southern Ocean and subtropical gyres, features for which the position, direction, and strength are in agreement include: (a) the eastward flow in the ACC and SIC or SPC, which are associated with cross-stream pressure differences of 50-80 dynamic centimeters (dcm); (b) the subtropical gyre in the central and eastern Pacific, including the eastern limb found 20° west of South America and an SEC with pressure differences of 5-7 dcm that flows west along 20°S before approaching Australia; (c) the strong EAC (~10 dcm) along Australia from 20°S to 35°S; (d) eastward flow across the Tasman Sea north of New Zealand which then flows south to join the SPC;

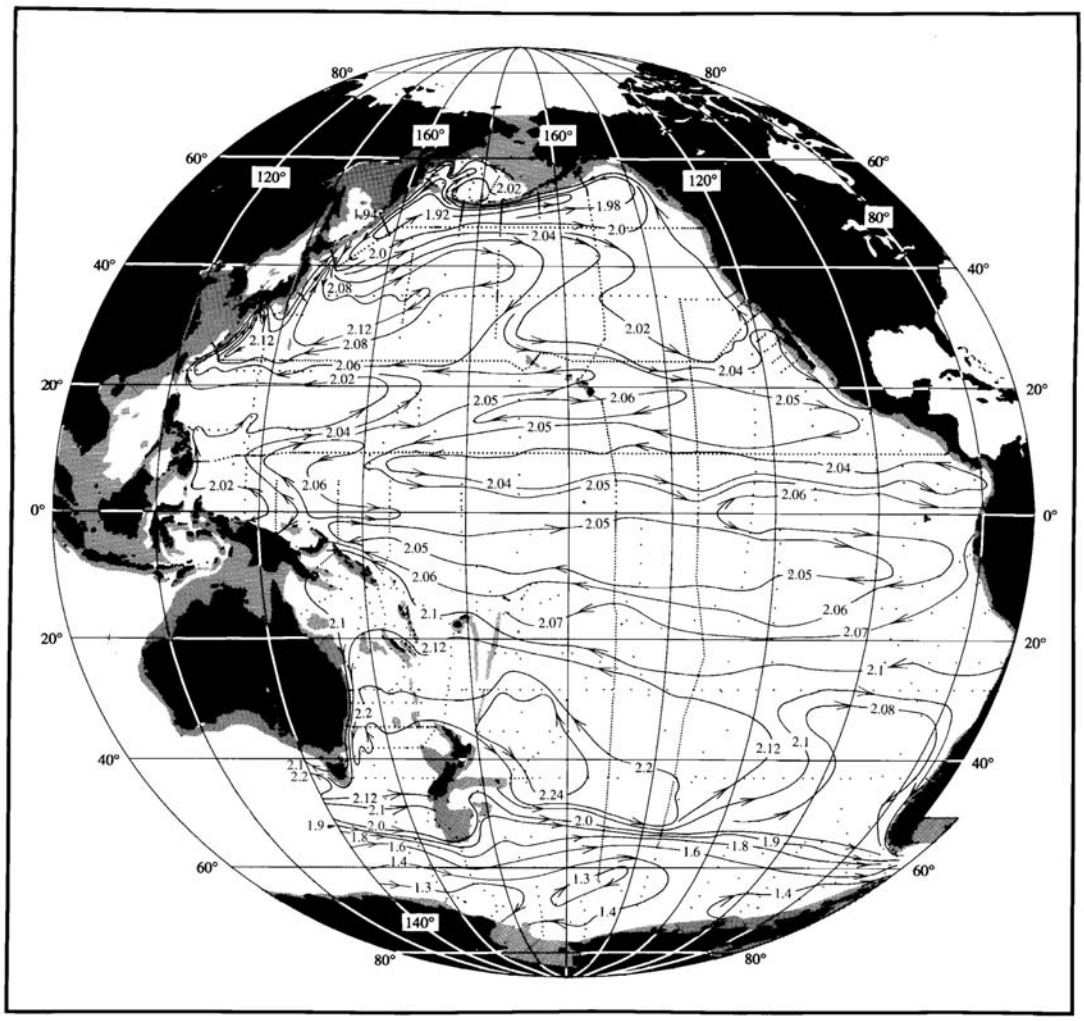

Figure E1. Adjusted mean steric height of the Pacific Ocean at 800 decibars from Reid (1997). Units are dynamic meters or 10 m^2s^{-2}.

(e) an extension of the EAC to Tasmania where it joins waters from the retroflected SIC and runs west into the Indian Ocean; (f) the entire Indian Ocean subtropical gyre including the Agulhas and SIC, the eastward extension south of Australia to the retroflection south of Tasmania and westward flow in a SEC; and (g) the split of the SEC around Madagascar, both branches feeding the Agulhas.

There are four significant differences between the float maps and Reid's analysis south of the tropical gyres. (1) In the Pacific the float SEC remains focused until it impinges on the Great Barrier Reef where part feeds the EAC and part turns north to feed a cyclonic gyre in the Coral and Solomon Seas. Reid's SEC grows more diffuse as it moves west, splits near 170°E with part directly feeding the EAC while more turns northwest to the east of the Solomon Islands. Some of this northwestward flow turns south to the east of New Guinea so that Reid's flow in the Coral and

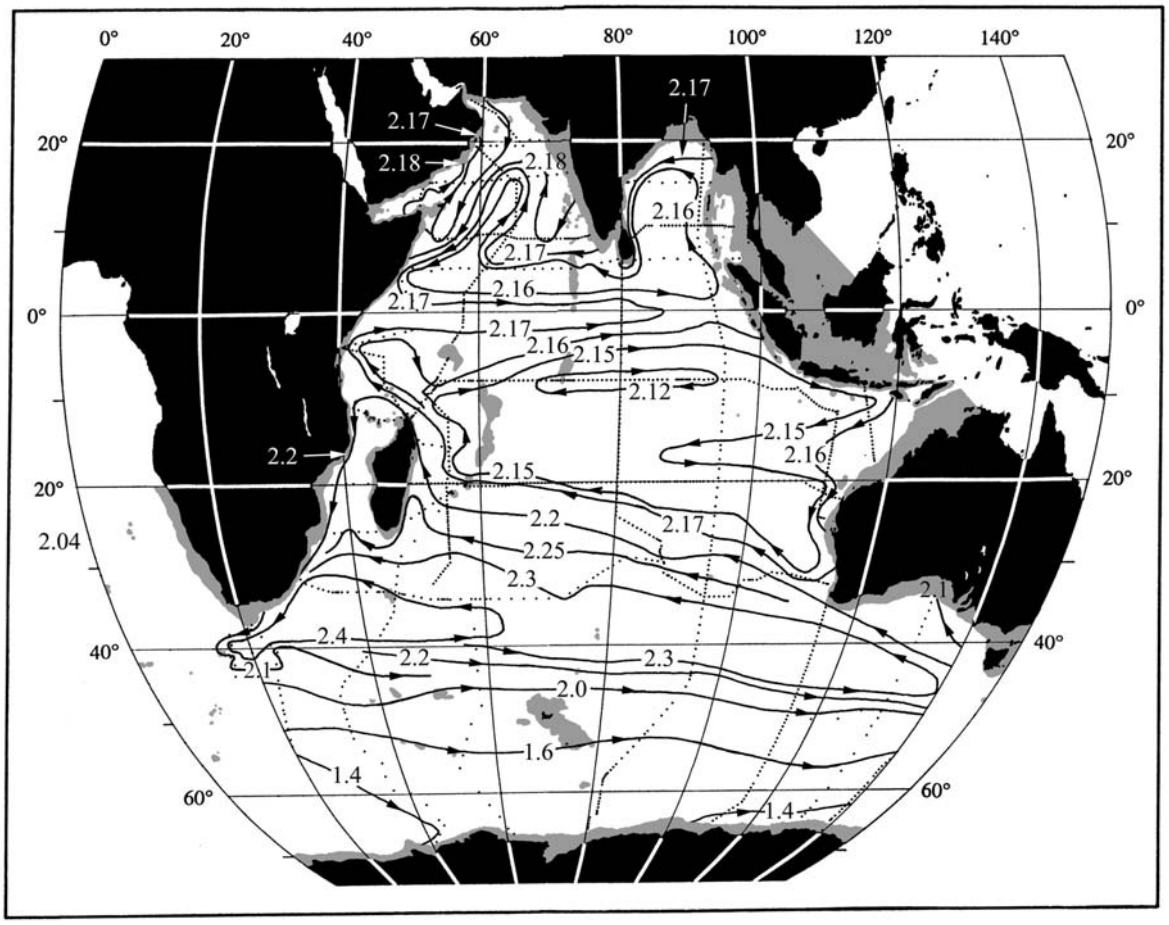

Figure E2. Adjusted mean steric height of the Indian Ocean at 800 decibars from Reid (2003). Units are dynamic meters or 10 m^2s^{-2}.

Solomon Seas is to the south. Using a much more dense hydrographic data set, Ridgway and Dunn (2003) show maps of dynamic height at 500 and 1200 m relative to 2000 m that also indicate cyclonic flow in the Coral and Solomon Seas. (2) There is little coherent pattern to float flow east of the Pacific's subtropical gyre (i.e. 85°W) whereas in Reid's picture some of the gyre's eastern limb doubles back to form a southward current along the Chilean coast. Float density is low here but flow across the float lines along 20°S and 85°W is negligible, which excludes any extension of a strong subtropical gyre to the boundary. (3) In the Indian Ocean the float subtropical gyre extends to lower latitudes than Reid's, allowing the SEC to impinge directly onto Madagascar. (4) Reid's analysis does not show the perturbations in the ACC/SIC that are ascribed in Figure 17 to the topographic influence of the Del Cano Rise and the Kerguelen Plateau, and he allows geostrophic flow into Campbell Plateau from the west whereas we have excluded this by design.

Differences between floats and Reid's analyses are greater in the tropics than in the subtropics. In both basins both analyses have northern and southern tropical cyclones separated by a pressure ridge along the equator supporting eastward equatorial flow. Reid's tropical gyres are stronger (near equatorial flows over 10 cm s^{-1}) than floats find. In the tropical Pacific the main differences are (a) smoother and stronger gyres in both hemispheres in Reid's analysis, (b) the high pressure ridge extending northeastward from western New Guinea extends to 20^{o}N in the float map while there is a low in this region between 10^{o}-20^{o}N in the hydrographic analysis, and (c) zonal pressure gradients along the equator and flow out of South America in Reid's analysis are absent in Figure 16. The pressure ridge in (b) neighbors a void in the float data and may be subject to significant sampling error. In the tropical Indian Ocean the main differences are that the hydrographic analysis shows (a) interior cross-equatorial flows not seen by floats, (b) a southern tropical gyre that extends farther south, (c) a complexity in the northern Arabian Sea that differs from the complexity in the float analysis there, and (d) a current with 1-2 dcm pressure difference that emanates from Sumatra (potentially carrying water southwestward from the Indonesian Throughflow) that is 3-5 times stronger than the equivalent transport found by floats (see Table 1).

References

Beal, L.M., and H.L. Bryden, 1999: The velocity and vorticity structure of the Agulhas Current at 32°S. *J. Geophys. Res.,* **104**, 5151-5176.

Boebel, O., R.E. Davis, M. Ollitrault, R.G. Peterson, P.L. Richardson, C. Schmid and W. Zenk, 1999: The intermediate depth circulation in the western South Atlantic. *Geophys. Res. Lett.*, **26**, 3329-3332.

Boebel, O., T. Rossby, J. Lutjeharms, W. Zenk and C. Barron, 2003: Path and variability of the Agulhas Return Current. *Deep-Sea Res.* II, **50**, 35-56.

Boning, C.W., 1988: Characteristics of particle dispersion in the North Atlantic: an alternative interpretation of SOFAR results. *Deep-Sea Res.*, **35**, 1379-1385.

Bower, A.S., B. Le Cann, T. Rossby, W. Zenk, J. Gould, K. Speer, P.L. Richardson, M.D. Prater, H.-M. Zhang, 2002: Directly-measured mid-depth circulation in the northeastern North Atlantic Ocean. *Nature*, **419**, 603-607.

Bretherton, F.P., R.E. Davis, and C.B. Fandry, 1975: A technique for objective analysis and design of oceanographic experiments. *Deep-Sea Res.*, **23**, 559-582.

Chapman, P., S.F. Di Marco, R.E. Davis and A.C. Coward, 2003: Flow at intermediate depths around Madagascar based on ALACE float trajectories. *Deep-Sea Res. II*, **50**, 1957-1986.

Davis, R.E., D.C. Webb, L.A. Regier and J. Dufour, 1991: The Autonomous Lagrangian Circulation Explorer (ALACE). *J. Atm. Oceanic Tech.*, **9**, 264-285.

Davis, R.E., 1998: Preliminary results from directly measuring mid-depth circulation in the tropical and South Pacific. *J. Geophys. Res.*, **103**, 24619-24639.

Davis, R.E., J.T. Sherman and J. Dufour, 2001: Profiling ALACEs and other advances in autonomous subsurface floats. *J. Atm. Oceanic Tech.*, **18**, 982-993.

Figueroa, H.A., and D.B. Olson, 1989: Lagrangian statistics in the South Atlantic as derived from SOS and FGGE drifters. *J. Mar. Res.*, **47**, 525-546.

Freeland, H.J., P.B. Rhines, and T. Rossby, 1975: Statistical observations of trajectories of neutrally buoyant floats in the North Atlantic. *J. Mar. Res.*, 33, 383-404.

Gille, S.T., 2003: Float observations of the Southern Ocean. Part I. Estimating mean fields, bottom velocities, and topographic steering. *J. Phys. Oceanogr.*, **33**, 1167-1181.

Gordon, A.L., E. Molinelli, and T. Baker, 1978: Large-scale relative dynamic topography of the Southern Ocean. *J. Geophys. Geophys. Res.*, **83**, 3023-3032.

Kamenkovich, V.M., 1962: On the theory of the Antarctic Circumpolar Current. *Tr. Instit. Okeanol.*, **56**, 241-293.

Lavender, K., R.E. Davis and B. Owens, 2000: Mid-depth recirculation observed in the interior Labrador and Irminger Seas by direct velocity measurements. *Nature*, **407** (7 Sept.), 66-69.

Lavender, K., B. Owens and R.E. Davis, 2004: Mid-depth circulation of the subpolar North Atlantic as measured by subsurface floats. *Deep-Sea Res.*, accepted.

Ocean Data Laboratory, 1998: World Ocean Atlas 1998. National Ocean Data Center, Silver Springs, Maryland.

Ollitrault, M., 1999: MARVOR floats reveal intermediate circulation in the western equatorial and tropical South Atlantic (30^oS to 5^oN). *WOCE Newsletter*, **34**, 7-10.

Owens, W.B., 1991: A statistical description of the mean circulation and eddy variability in the northwestern Atlantic using SOFAR floats. *Prog. Oceanogr.*, **28**, 257-303.

Richardson, P.L., and S.L. Garzoli, 2003: Characteristics of Intermediate Water flow in the Benguela Current as measured by RAFOS floats. *Deep-Sea Res II.*, **50**, 87-118.

Ridgway, K.R., and J.R. Dunn, 2003: Mesoscale structure of the mean East Australian Current System and its relationship with topography. *Prog. Oceanogr.*, **56**, 189-222.

Riser, S.C., 2004: Lagrangian observations of the mid-depth circulation in the western North Pacific. *In preparation.*

Reid, J.L., 1997: On the total geostrophic circulation of the Pacific Ocean: flow patterns, tracers, and transports. *Prog. Oceanogr.*, **39**, 263-352.

Reid, J.L., 2003: On the total geostrophic circulation of the Indian Ocean: flow patterns, tracers, and transports. *Prog. Oceanogr.*, **56**, 137-186.

Roemmich, D., and P. Sutton, 1998: The mean and variability of ocean circulation past northern New Zealand: determining the representativeness of hydrographic climatologies, *J. Geophys. Geophys. Res.*, **103**, 13041-13054.

Roemmich, D., and W.B. Owens, 2000: The Argo Project: global ocean observations for understanding and prediction of climate variability. *Oceanography*, **13**, 45-50.

Rossby, H.T., S.C. Riser and A.J. Mariano, 1983: The western North Atlantic – a Lagrangian viewpoint, pp 66-91 in *Eddies in Marine Science,* ed. A.R. Robinson, Springer-Verlag, Berlin.

Stammer, D., C. Wunsch, R. Giering, C. Eckert, P. Heimbach, J. Marotzke, A. Adcroft, C.N. Hill and J. Marshall, 2003: Volume, heat, and freshwater transports of the global ocean circulation 1993–2000, estimated from a general circulation model constrained by World Ocean Circulation Experiment (WOCE) data. *J. Geophys. Res.* Vol. **108**, DOI 10.1029/ 2001JC001115

Swallow, J.C., 1955: A neutral-buoyancy float for measuring deep currents. *Deep-Sea Res.,* **3**, 74-81

Taylor, G.I., 1921: Diffusion by continuous movements. *Proc. Lond. Math. Soc.*, **20**, 196-212.

Wijffels, S.E., J.M. Toole and R. Davis, 2001: Revisiting the South Pacific subtropical circulation: A synthesis of World Ocean Circulation Experiment observations along 32^oS. *J. Geophys. Res.*, **106**, 19481-19513.

Figure Captions

Figure 1. Float coverage in the Pacific. Each subsurface displacement (usually over 25 days) is shown as an arrow. All displacements from one float are in the same color. Depths less than 3000 m are shaded and those less than 700 m are shaded more darkly.

Figure 2. Float coverage in the Indian Ocean. Format is as in Figure 1.

Figure 3. Raw subsurface float displacements (arrows) near New Zealand. Most displacements are over 25 day intervals near 900 m depth. All displacements from a float are in the same color. Land and depths less than 700 and 3000 m are shaded. Features are (a) southward flow along the North Island toward Chatham Rise in an intermediate-depth analog of the East Auckland Current, (b) westward flow north of Campbell Plateau that turns eastward along Chatham Rise, and (c) confused flow west of New Zealand. One float (cyan) is captured by and grounded on an eddy over the Lord Howe Rise (39^oS, 169^oE) while another (magenta) becomes grounded southeast of this feature.

Figure 4. Raw trajectories around the Coral Sea and New Guinea in the format of Fig. 3. Flow enters the Coral Sea near 17^oS, follows the western boundary around the Coral Sea and tip of New Guinea. One float (yellow) travels north-westward at speeds over 15 cm s^{-1} along the New Guinea coast while others escape the Solomon Sea to the east and through the Solomon Islands. Flow is toward the equator east of the Solomon Islands. Equatorial flow is zonal but in both directions, so the sense of mean flow cannot be determined without averaging.

Figure 5. Raw data near Madagascar. Note (a) a bifurcation on the east coast of Madagascar that feeds a southward boundary current, which feeds the Agulhas and a northward flowing eastern boundary current in the Mozambique Channel, (b) a flow north from the bifurcation that then flows west to Africa, (c) a southward boundary current along the African coast, including Mozambique Channel, and (d) an anti-cyclonic eddy in the northern Channel encompassing the southward boundary current along Africa and the northward boundary current along the west coast of Madagascar.

Figure 6. Raw displacements around South Africa. In the northeast corner of the figure is the flow south of Madagascar (Figure 5). Peak speeds in the intermediate-depth Agulhas Current exceed 50 cm s^{-1}. Note the rapidity with which this current accelerates and decelerates. The frequency of eastward flow along 40^oS suggests a retroflection of this current while confused flow west of Africa suggests flow into the Atlantic.

Figure 7. Velocity of the dominant EOFs for the Indian (left) and Pacific Oceans (right) from the JPL-ECCO data-assimilating numerical model (courtesy Dr. Benyang Tang). Each EOF is scaled so its speed equals the standard deviation of the velocity it explains. Velocities less than 1 cm/s are in green using the scale at the upper left. Speeds between 1 and 2 cm/s are in blue and above 2 cm/s is in red.

Figure 8. Seasonal cycle of EOF amplitudes for the Indian (left) and Pacific Oceans (right). Solid lines are the amplitudes of the first three most energetic EOFs when fit to float velocities. Dashed lines are the amplitudes of these modes in the JPL/ECCO data-assimilating model.

Figure 9. Lagrangian time-lagged correlation of east velocity *u* (solid) and *v* (dashed). Bins are 25 days. The zero-lag bin includes some non-zero-lag pairs. Data from the Indian and South Pacific Oceans is combined. Area-average mean velocities (Figs. 10 and 11) were removed, as were the 4-EOF annual cycles in each ocean.

Figure 10. Area-average mean velocity at 900 m in the Pacific Ocean from 1332 float-years of data using parameters R_{AV} = 300 km and μ =300 km. Arrows show speed and direction at the arrow's base on a nominal 3° grid. Speeds $|\mathbf{u}| < 1$ cm s^{-1} are plotted in green using the green scale at the top. Blue is for 1 cm s^{-1} < $|\mathbf{u}|$ < 3 cm s^{-1}. Red is used when $|\mathbf{u}| > 3$ cm s^{-1}. Shading denotes the 900 m and 3000 m isobaths in the bathymetry, smoothed to one-degree resolution, used in shaping the averaging cells.

Figure 11. Area-average mean flow at 900 m in the Indian deduced from 1291 float-years of data using parameters R_{AV} =300 km and μ =300 km. Format is as in Figure 10.

Figure 12. Mean velocity vectors with sampling error ellipses at their base for 900 m depth in the Pacific calculated by fitting to 5 functions of constant or linearly sheared nondivergent velocity over an area with radius R_{FIT} = 300 km. Three color-coded scales are used: green for mean speed $q < 1$ cm s^{-1}; blue for $1 < q < 3$ cm s^{-1}; red for $q > 3$ cm s^{-1}. From north to south, the elements of the circulation are (a) in the western Pacific north of 20°N, an eastward flow of O(1 cm s^{-1}) that apparently receives flow from the intermediate-depth North Equatorial Current (NEC); (b) a westward NEC west of 140°W along 10°N; (c) a generally eastward flow along the equator apparently fed from the equatorward flow east of New Guinea; (d) a westward intermediate depth South equatorial Current (SEC) that crosses the basin at 20°S in the east and 20°S in the west; (e) flow from the SEC northwestward into the Coral Sea to feed the equatorward flow past New Guinea and southward along Australia in an intermediate depth East Australia Current (EAC); (f) eastward flow from the EAC past the north of New Zealand and then southeastward to join the strong eastward flow south of 50°S; (g) a strong eastward flow between 50°S and 60°S that comprises the Antarctic Circumpolar Current (ACC) and the poleward branch of the subtropical gyre, the South Pacific Current (SPC); (h) the northward flowing eastern branch of the subtropical gyre centered near 100°W; (i) westward current south of Australia apparently partly fed by the EAC but mainly from retroflection of the eastward flow to the south, which Figure 13 indicates is the eastern limb of the Indian Ocean's subtropical gyre; and (j) a flow south from the ACC toward the eastern Ross Sea near 135°W .

Figure 13. Mean flow and error ellipses for the Indian Ocean at 900 m in the format of Fig. 12. Flow north of the equator is confused except for westward flow out of the Bay of Bengal and past the tip of India and trans-equatorial flow in the eastern equatorial zone that appears to feed a weak but distinct southeastward flowing boundary current along the Indonesian Archipelago. This boundary current is the eastern limb of a tropical gyre that includes a westward South Equatorial Current (SEC), an intermediate-depth Somalia Current along Africa, and eastward flow along the equator. There is no evidence of the Great Whorl in the Arabian Sea. Most of the SEC feeds the subtropical gyre through southwestward flow east of Madagascar and a smaller flow north of Madagascar that then passes southward through the western Mozambique Channel. Both sources feed an intermediate-depth Agulhas Current that accelerates to speeds over 20 cm s^{-1}. Most of the

Agulhas retroflects to the east along 40°S to form a South Indian Current (SIC) that appears to be distinct from the ACC west of 80°E. The eastern limb of the subtropical gyre may extend as far as 145°E before turning back to feed the Tasman Current south of Australia. This westward flow might be regarded as the SEC displaced south of its equilibrium by the continent that is also fed from the EAC and thus represent an inter-basin flow. Passing Australia the SEC drifts equatorward to 20°S where it impinges on Madagascar. It is difficult to separate possible flow through Indonesian Seas from the eastern parts of the tropical and subtropical gyres. Similarly, east of Africa it is difficult to tell how much of the northwestward flow is an inter-basin flow from the Agulhas.

Figure 14. Ellipses of eddy diffusivity K_{ij} at 900 m in the Pacific computed from (7). Ellipse axes (diameters) are proportional to the principal axes of the diffusivity according to the color-coded scales at the top. The diffusivity is large and highly anisotropic in the equatorial zone where zonal dispersion dominates. Otherwise *K* is approximately isotropic. Other regions of high eddy variability are the ACC, EAC and Tasman Current.

Figure 15. Single-particle eddy diffusivity at 900 m in the Indian Ocean in the same format as Fig. 14. Equatorial variability is anisotropic but less so than in the Pacific. The patterns of eddy diffusivity are analogous to those in the Pacific although generally stronger in the Indian Ocean. Variability is greatest in the "overshoot" region of the Agulhas, not where the velocity is greatest.

Figure 16. Objectively mapped geostrophic pressure (in centimeters of water, equivalent to dynamic centimeters) for the Pacific Ocean. The irregular contour values are listed over South America. The ridge along 15°N supports a confused intermediate-depth NEC, which apparently feeds the equator without reaching the western boundary. An equatorial ridge separates cyclonic tropical gyres in both hemispheres and supports eastward equator flow {6/6}. The southern tropical gyre is interrupted by a high just west of the East Pacific Rise (EPR) {5/6}. A strong cyclone in the Coral and Solomon Seas {6/6} feeds a weak flow to the equator well east of New Guinea {4/6}. The eastern limb of the subtropical gyre is well west of South America {5/6}. This limb separates from the SPC/ACC between 245° and 260°E over the EPR {5/6}. The East Australian Current (EAC) is strongest at latitudes north of New Zealand but a weaker current flows south past Tasmania and then west into the Indian Ocean, just south of Australia {6/6}. Most of the EAC turns east near 35°N, flowing past New Zealand and then along its east coast to join the ACC at 45°S over Chatham Rise {6/6}. There is a weak cyclonic eddy in the Tasman Sea, some of which feeds the subtropical circulation by flowing south of New Zealand {5/6}. Some eastward flow in the SIC (or ACC) retroflects south of the Tasman Sea and returns to the Indian Ocean (see also Figs. 15 and 17).

Figure 17. Objectively mapped geostrophic pressure (cm of water) for the Indian Ocean. Lows in the Bay of Bengal {6/6}, the Arabian Sea {5/6}, and the tropical gyre south of the equator support eastward flow along the equator {6/6}. Both tropical gyres include western boundary currents along Africa {6/6}. A weak Indonesian Throughflow {6/6} augments westward flow south of Australia to form an SEC that bifurcates on Madagascar {6/6}. Most of the SEC turns south along Madagascar and crosses the Mozambique Channel to form the intermediate-depth Agulhas. The rest of the SEC flows north around Madagascar and forms a western boundary current in the Mozambique Channel that adds to the Agulhas {6/6}. The Agulhas accelerates sharply, overshoots Africa and retroflects to form the SIC but some escapes into South Atlantic in a stream that separate immediately from the African Coast {6/6}. (The band of pressures between 0 and 5 cm marked yellow that continues

along the African east coast is lost in the graphic). The ACC/SIC splits behind Del Cano Rise (45^{o}E) and refocuses behind the Kerguelen Plateau (70^{o}E), flows south of Australia before some retroflects south of the Tasman Sea {6/6} as shown in Fig. 16. Some the South Atlantic Current flows east past the tip of Africa, retroflects south of the Tasman Sea, and re-enters the Atlantic from the Agulhas, making Campbell Plateau (50^{o}S, 170^{o}E) the eastern boundary for part of the South Atlantic's subtropical gyre.

Figure D1. Streamfunction for Pacific Ocean mean circulation at 900 m. Units are 1000 m^2s^{-1} and streamfunction differences correspond to transport per unit depth. Contour interval is 5000 m^2s^{-1} with additional contours at $\pm$ 2000 m^2s^{-1}.

Figure D2. Streamfunction for Indian Ocean mean circulation at 900 m. Contours are labeled in units of 1000 m^2s^{-1} with an interval of 5000 m^2s^{-1} plus contours at $\pm$ 2000 m^2s^{-1}.

Figure E1. Adjusted mean steric height of the Pacific Ocean at 800 decibars from Reid (1997). Units are dynamic meters or 10 m^2s^{-2}.

Figure E2. Adjusted mean steric height of the Indian Ocean at 800 decibars from Reid (2003). Units are dynamic meters or 10 m^2s^{-2}.